Journal of Nuclear Materials 620 (2026) 156311

Contents lists available at ScienceDirect

Journal of Nuclear Materials

journal homepage: www.elsevier.com/locate/jnucmat

The impact of the matrix and buffer properties on residual stresses in TRISO particles during manufacture and early life

Udeme Inyang-Udoh [a], Angelo Battistini [b], Lloyd Jones [c], Alex Leide [d], Mark R. Wenman [b], Thomas A. Haynes [a,b,*]

[a] University of East Anglia, Norwich Research Park, Norwich, Norfolk, NR4 7TJ, United Kingdom
[b] Imperial College London, Centre for Nuclear Engineering, South Kensington Campus, London, SW7 2AZ, United Kingdom
[c] United Kingdom National Nuclear Laboratory (UKNNL), NNL Preston Laboratory, Springfields Works, Salwick, Preston, Lancashire, PR4 0XJ, United Kingdom
[d] UK Atomic Energy Authority, Culham Science Centre, Abingdon OX14 3DB, United Kingdom

ARTICLE INFO

Keywords:
TRISO
Residual stress
High temperature reactor
Fuel performance
Modelling

ABSTRACT

A three-dimensional finite-element model was developed using Abaqus to simulate the fabrication and initial power ramp-up of a tri-structural isotropic (TRISO) particle, featuring a UO_2 kernel, encapsulated in either a SiC or graphite matrix. After sintering, the residual compressive hoop stress in the SiC coating layer reached -540 MPa when encapsulated in a graphite matrix, 94 MPa more compressive than in a SiC matrix. However, following the initial power ramp-up, the predicted compressive hoop stresses in the SiC layer of a particle embedded in a SiC matrix (-388 MPa) were significantly greater than in a graphite matrix (-222 MPa), emphasizing the matrix material's critical role in the stress state of the SiC layer. Model validation attempts were made with the experimental measurements of the residual stresses of a zirconia-kernel surrogate particle. We found that in a fully-bonded surrogate TRISO particle, the stress state of the SiC layer is highly sensitive to the buffer porosity with compressive SiC layer hoop stresses ranging from up to -1.06 GPa at a porosity of 0.14 to -0.77 GPa at a porosity of 0.60. Partial kernel/buffer delamination simulations revealed a significantly varied geometric stress distribution, with tensile stresses reaching up to +54 MPa and compressive stresses up to -546 MPa at different axes of the sectioned plane in the model. This finding suggests that contrary to the common assumption of complete delamination at the kernel/buffer interface during fabrication, partial delamination is a more plausible explanation for the high compressive stresses observed in the SiC layer experimentally.

1. Introduction

At the heart of high-temperature reactor (HTR) designs is tri-structural isotropic (TRISO) fuel, chosen for its excellent structural integrity and chemical stability during irradiation and accident scenarios [1]. The Advanced Gas Reactor (AGR) programme fuel qualification irradiation campaigns (AGR-1 and AGR-2) have demonstrated its potential for use in HTRs, with SiC failure rates of 1 in 103,000 and TRISO failure rates of 1 in 52,000 particles [2]. TRISO fuel kernels have conventionally been produced using either uranium dioxide (UO_2) [3] or uranium oxycarbide (UCO), a mixture of uranium carbide (UC) for its high thermal conductivity and UO_2 for chemically stability due to the presence of oxygen [4]. More unconventional TRISO fuel kernel types have been proposed such as uranium nitride (UN), that allows for a higher uranium density (which increases the fissionable nuclei) and higher thermal conductivity which leads to lower temperature gradients in the kernel [5].The SiC layer has performed significantly better than expectation in the AGR tests, failures primarily due to diffusion and sparsely with cracks propagating from the other layers of the particle. In the United States and Canada, TRISO fuel with a UCO kernel is currently the selected choice due to its excellent safety performance at high temperatures during the irradiation and accident safety tests of AGR-1 and AGR-2 [2]. One of the factors affecting the particle failure rate may be due to the presence of significant compressive residual stresses in the layers of the particle after manufacture. TRISO particles are typically fabricated using fluidized bed chemical vapor deposition (FB-CVD), a thermally driven process where precursor gases are introduced, react, and decompose to deposit thin, uniform coatings onto substrates. As the

* Corresponding author.
E-mail address: t.haynes@uea.ac.uk (T.A. Haynes).

https://doi.org/10.1016/j.jnucmat.2025.156311
Received 11 August 2025; Received in revised form 17 November 2025; Accepted 18 November 2025
Available online 19 November 2025

coatings are formed at high temperatures before cooling down, it is expected that the difference in thermal expansion of the various layers lead to a complex stress profile in the layers of the particle. However, most fuel performance codes model the particle as stress-free at the start of its service life [6–9]. Recently, work by Battistini et al. [10] and Leide et al. [9] showed that there are significant tensile stresses in the PyC layers and compressive stresses in the SiC layer. The compressive stresses in the SiC layer may lead to results of PIE investigations that scarcely show SiC failure.This work adopts a similar approach to Battistini et al. [10] in simulating TRISO coating deposition, but employs contact interaction techniques to examine the interfacial behaviour between the coating layers.

A study of the residual stresses in TRISO particles was first published by Martin [11] using analytical calculations using a range of thermal expansion coefficients of the layers in the particle layers. The study found that stresses during deposition remain relatively minimal, while the stress distribution after cooling exhibits great variability and uncertainty, dependent on the thermal expansion coefficients of the three outermost layers across the temperature range of 5 to 2000 °C. There have been other studies that examine residual stresses, the results of which are presented in Table 1 in chronological order and show a wide range of predicted measured stress state with most studies predicting or observing compressive stresses in the SiC layer. Despite these efforts, no clear consensus has emerged within the TRISO fuel performance literature regarding the magnitude or nature of these stresses, owing to the limited availability of high-temperature material property data for TRISO constituents and the scarcity of experimental investigations into the complex stress fields that may develop after fabrication. Furthermore, uncertainties persist regarding how these stress fields evolve under the influence of characteristics and phenomena such as delamination, surface roughness, microstructural evolution, and chemical interactions.

Table 1
Summary of Literature on Residual Stress and Strain Measurements of TRISO Fuel.

Study	Particle Type	Method	Summary of Results
Martin [11] 1975	UO_2 kernel	Analytical	"Modest" stresses (±30 MPa) in all layers during deposition with maximum possible stress in SiC at −300 MPa after cool down.
Tan et al. [12] 2008	~530 μm diameter yttria-stabilized ZrO_2 surrogate kernel	Electron backscatter diffraction (EBSD)	"Significant" strain zones in columnar grains in SiC layer.
Kirchhofer et al. [13] 2010	Unknown surrogate kernel ~500 μm	Raman spectroscopy and EBSD	SiC layer both in tension and compression depending on the direction of Raman Shift measurement but dominant tensile stresses in SiC layer.
Kirchhofer et al. [14] 2013	Zirconia kernel of ~530 μm diameter	EBSD	Low misorientation angles are indicative of insignificant residual stress in SiC layer.
Battistini et al. [10] 2023	German AVR TRISO with UO_2 kernel	Finite element modelling (ABAQUS)	Compressive hoop stress of up to −675 MPa in SiC layer, up to +56 MPa in IPyC layer and up to +30 MPa in OPyC layer. In debonded case, compressive hoop stresses of up to −150 MPa in the SiC layer.
Leide et al. [9] 2023	USNC particle with Zirconia kernel	Focussed ion beam digital image correlation	Compressive hoop stress up to −785 MPa in SiC layer and +78 MPa in IPyC layer, and +58 MPa in OPyC layer.
Montoya et al. [15] 2025	US AGR-2 particle	Finite element modelling (BISON)	Compressive hoop stresses of up to −380 MPa in SiC layer, tensile hoop stresses of up to +50 MPa in IPyC layer and +30 MPa in OPyC layer in fully bonded model.

A common factor in these studies is that none of them explore the residual stress factoring in the encapsulating matrix. Nevertheless, there have been a few studies in literature that study the encapsulating matrix when exploring the fuel performance in reactor transients [16–20].To the authors' best knowledge, no study has modelled a matrix-encapsulated TRISO particle's residual stresses and its initial power ramp-up Also, the authors have found no study that explores how the choice of the matrix material and its characteristic sintering conditions may affect the stresses experienced in the particle during manufacture and at the start of the TRISO particle service life. This work explores these gaps in the TRISO fuel performance literature.

Furthermore, it is well-established that on irradiation of the particle, the micromechanical properties of the buffer layer cause separation between the buffer and the IPyC layer, a critical and frequently observed phenomenon in TRISO fuel performance [21–24]. This has drawn a lot of attention to the buffer, a layer with traditionally higher manufacturing tolerances than the rest of the particle [25]. Recent studies have shown significant heterogeneity in the buffer's mechanical properties [26]. In this study, we explore the impact of the buffer porosity during the fabrication process of the fuel on the residual stress in the coating layers. Our study explores the gaps between the results obtained by experimental measurements of these residual stresses by modelling the manufacture of TRISO particles with a surrogate ZrO_2 kernel. The surrogate model developed is used to validate the method in this study and provides opportunities for further analysis on interfacial effects on the stress distribution of the particle during and after manufacture.

2. Methodology

2.1. Model description

The model, developed in Abaqus 2023, aims to capture the evolution of mechanical strains during the manufacture and initial rise to power for a single TRISO particle and surrounding matrix. The simulated manufacturing process including the coating deposition temperatures, that may have an influence on the stress state of the layers in the manufacturing transient, was based upon that used for the AGR fuel qualification programme [27].

To capture and explore interfacial interactions during the manufacturing process, a surface-to-surface cohesive contact was used as compared to the "tie" constraint that was used by Battistini et al. [10]. Manufacture is represented by a series of steps. Parts representing each layer in the fuel are introduced in a stress-free state at their deposition temperature with no thermal strain. The dimensions of the overlaying layer at the point of deposition were adjusted to match the strained dimensions of the underlaying layer at the point of deposition as shown in Eq. (1). A schematic of the process is shown in Fig. 1. It was assumed that since the particle is relatively small, the deposited layers uniformly and instantly reach the temperature of the coating gas for the next deposition step. Hence, at deposition of each of the layers, the thermal gradient between the substrate and the coating layer is zero.

$$\boldsymbol{r_{i,d} = r_{o,s} + d_{c/e}} \tag{1}$$

Where $r_{i,d}$ is the inner radius of the deposited layer, $r_{o,s}$ is the outer radius of the substrate layer and $d_{c/e}$ is the radial displacement due to expansion or contraction of the substrate layer

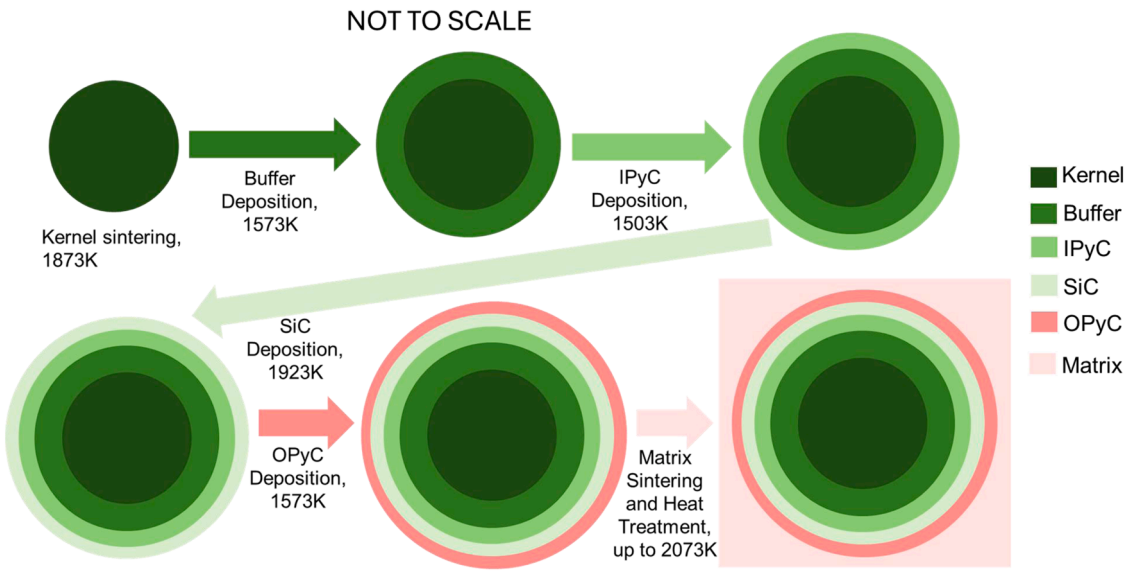

Fig. 1. Schematic of the simulated manufacturing process.

2.2. Particle geometry

The model was built to represent a single TRISO particle inside a matrix with dimensions given in Table 2. To study the effect of symmetry and boundary conditions imposed on the matrix, we simulated both spherical and cuboidal matrices which is extensively discussed in Section 2.6. Symmetry was exploited to minimise computational demand and therefore only an eighth of the cube and sphere were modelled, as shown in Fig. 2. The kernel diameter and layer thicknesses are appropriate to the AGR-2 experiments [28,29]. For a cuboidal matrix, the particles are assumed to be packed in a body centred cubic (BCC) lattice. The matrix length is determined analytically by estimating the pitch, a, of the lattice, aligned to a volumetric packing fraction, p, of 0.37 [29] for the AGR-2 TRISO particle (see Eq. (4)). The volume of the cuboidal matrix can then be defined as,

$$\boldsymbol{V_c} = (\boldsymbol{a} + 2\boldsymbol{r})^3 \tag{2}$$

Where r is the radius of the entire TRISO particle. Thus,

$$\frac{m}{6}\pi r^3 + \frac{4n}{3}\pi r^3 = p\left((a + 2r)^3\right) \tag{3}$$

Where m is the number of particles at edge of the lattice structure 8 and n is the particle at the body centre of the lattice structure. Thus,

$$\boldsymbol{a} = \left[\left(\frac{8\pi}{3\boldsymbol{p}}\right)^{1/3} - 2\right]\boldsymbol{r} \tag{4}$$

Similarly, the radius, R, of the spherical matrix is given by Eq. (5),

Table 2
The geometry assumed for a typical TRISO fuel particle embedded in a cube of matrix [28,29].

Dimension	AGR-2 Value (μm)
Kernel Radius	212.5
Buffer Thickness	100.0
Inner PyC Thickness	40.0
SiC Thickness	35.0
Outer PyC Thickness	40.0
Matrix Sphere Thickness	168.0
Matrix Block Width	948.0

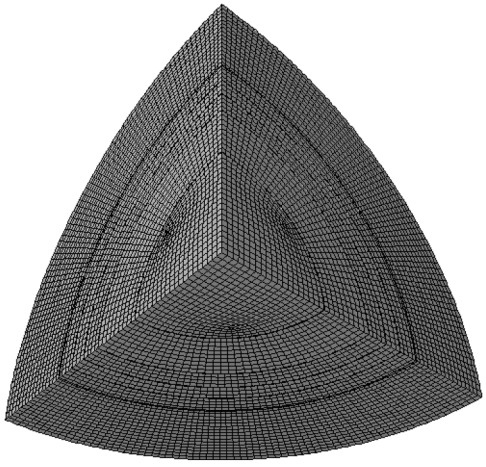

Fig. 2. Selected simulation mesh showing TRISO particle embedded in a spherical matrix material.

$$\boldsymbol{R} = \left(\frac{\boldsymbol{r}^3(1+\boldsymbol{p})}{\boldsymbol{p}}\right)^{1/3} \tag{5}$$

2.3. Mesh and computational demand

The physical domain was discretized using hexahedral coupled-temperature quadrilateral elements (C3D20RT) with an average edge length of 11 μm as shown in Fig. 2. The sizes of the discretized elements are greater than the average grain sizes of typical TRISO particle layers which are usually below 10 μm^2 [30,31], keeping continuum mechanics assumptions valid. The mesh consisted of 101,215 elements. In the case of partial debonding simulations, tetrahedral-shaped elements were used to capture the boundaries between the bonded and de-bonded regions of the kernel/buffer interface. The simulations were performed using an implicit finite element solver on a high-performance computing cluster of 32 cores and 160 GB of memory. Typical simulations required between 10 and 74 h for each of the transient solutions to converge.

2.4. Simulation steps, loads & boundary conditions

Table 3 lists the steps used to simulate manufacture of the TRISO particles; Table 4, to simulate encapsulation in a SiC matrix; and Table 5, to simulate encapsulation in a graphite matrix. The temperatures shown in these models were only applied to 'active' parts [or materials] in each step. Table 3 is based on the deposition temperatures and coating rates described by Seibert et al. [27]; sintering conditions in Table 4 are based on those reported by Terrani et al. [32] and Table 5 is based on the study by Hunn [29]. The technique used for the deposition and bonding of all layers was the cohesive, rough (infinite coefficient of friction), hard, surface-to-surface contact interaction, allowing for no separation upon bonding of the layers. The first set of simulations do not implement a fracture criterion in the case that there are significant enough stresses to break the bonds at the interfaces. During the manufacture of the particle, strain was constrained to the radial direction; displacement in the tangential and azimuthal directions were therefore set to zero. This was done to allow for azimuthal uniformity during the expansion of the substrate layer to allow for the maximum possible contact with the subsequent deposited layer. This boundary condition was imposed exclusively during the deposition process. In practical manufacturing, the deposited layers deviate from perfect sphericity and Battistini et al. [10] demonstrated that such geometric imperfections may have a moderate influence on the residual stress distribution resulting from the fabrication process.

In the fabrication of Fully Ceramic Microencapsulated (FCM) fuel pellets, where TRISO particles are typically embedded in a SiC matrix, the compaction process may be sintered under uniaxial loads [33]. In contrast, conventional graphite matrices used in prismatic fuel compacts are typically formed via uniaxial pressing, whereas pebble-bed fuel forms generally employ near-isostatic pressing techniques [34]. In this study, the compaction process was idealized by applying a hydrostatic load equivalent to the pressing pressures specified in Table 4 and Table 5 on the outer surface of the matrix material. This simplified modelling approach was adopted to minimize complications arising from matrix-tooling interaction, focusing instead on the stress states experienced by a representative TRISO particle located away from the matrix/die interface. In practice, however, TRISO particle compaction is likely to involve highly non-uniform pressure distributions, as individual particles experience varying stresses depending on their position and orientation within the compact during sintering. The approach used here neglects discontinuities and contact effects which would otherwise arise at the interfaces. Also, it does not capture the complex mechanical phenomena typically associated with compaction, such as particle rearrangement, reorientation, and localized stress heterogeneity as the compact undergoes densification and shrinkage.

To model the initial rise to power, a temperature boundary condition was applied to the outside (or inter-particle plane) and a volumetric heat flux to the kernel. The temperature was linearly increased from 293 to 1305 K on the outer surface of the matrix and the kernel power simultaneously from 0 to 0.3 W; these values were based upon the fuel volume averaged temperature in the AGR-2 experiment [35] and previous models for kernel temperatures during the initial power ramp [6,36].

Table 4
Steps applied to simulate encapsulation in a SiC matrix.

Step	Duration (s)	Initial Temperature (K)	Final Temperature (K)
Matrix and TRISO in contact	100	293	293
TRISO hot pressed in SiC matrix at 20 MPa	7200	293	2123
Entire fuel form cool-down	7200	2123	293

Table 5
Steps applied to simulate encapsulation in a graphite matrix.

Step	Duration (s)	Initial Temperature (K)	Final Temperature (K)
Matrix and TRISO in contact	100	293	293
Warm press of fuel at 60 MPa	3600	293	368
Carbonization	13,100	368	1223
Entire compact cool down	3600	1223	293
Heat treatment of compact	9075	293	2123
Entire compact cool down	5475	2123	293

2.5. Material properties of TRISO fuel

There is a vast body of literature on the material properties of TRISO fuel materials. However, much of this information is outdated and often based on bulk materials rather than FB-CVD materials, which can exhibit different properties [37,38]. Additionally, the curvature of the deposition process may impact crystal structures, grain sizes, and layer compositions, ultimately influencing both thermal and mechanical properties. Pomeroy et al. [39] shows that reported values for the thermal conductivity of SiC can vary by close to two orders of magnitude. Although, the temperature-dependent change in the coefficient of thermal expansion of the SiC appears to plateau at around 1200 K, there are no reported experimental values of the thermal expansion of the material above 1500 K [37]. In such cases, the models are based on statistical inference. To develop higher fidelity models, curved FB-CVD material properties of the layers from room temperature up to 2150 K are needed. Neutron fluence dependence was not considered for the properties of the fuel as the dose is negligible in the early stage of the reactor operation. This will be considered in the future work on long-term fuel performance. It was also assumed that the kernel and coating layers of the particle behave isotropically in all conditions.

Also, graphitization of the PyC layers is likely to occur during heat treatment of the compact. Hunn et al. [40] reported that both the anisotropy and density of the PyC layer in TRISO particles increase with

Table 3
Steps applied to simulate TRISO manufacture and parts [or materials] active at each step.

Step	Duration (s)	Initial Temperature (K)	Final Temperature (K)	Kernel	Buffer	IPyC	SiC	OPyC
Kernel sintering	3600	1873	1873	✓				
Kernel ramp to buffer deposition temperature	100	1873	1573	✓				
Buffer Deposition	750	1573	1573	✓	✓			
Deposited layers ramp to IPyC deposition temperature	100	1573	1503	✓	✓			
IPyC deposition	1090	1503	1503	✓	✓	✓		
Deposited layers ramp to SiC deposition temperature	100	1503	1923	✓	✓	✓		
SiC deposition	10,500	1923	1923	✓	✓	✓	✓	
Deposited layers ramp to OPyC deposition temperature	100	1923	1573	✓	✓	✓	✓	
OPyC deposition	600	1573	1573	✓	✓	✓	✓	✓
TRISO cool down	7200	1573	293	✓	✓	✓	✓	✓

heat treatment, reflecting a progression toward a more graphitic structure. Such microstructural evolution will potentially reduce the PyC elastic modulus substantially. The extent and nature of these changes are highly dependent on the texture of the PyC layers and may also be influenced by the TRISO particle's physical and chemical environment [41,42]. In the present study, the effects of graphitization are not considered, primarily due to limited data and correlations on its impact on the material properties of PyC within a TRISO environment. Future investigations will focus on the implications of this phenomenon on TRISO fuel performance.

Tables 6 and 7 give the density and porosity for each material and layer in the model.

Correlations for the elastic modulus, E, as function of temperature, T and porosity, P are given in Table 8. The values of Poisson's ratio are given in Table 9. After considering the relative porosity, the properties of the graphite matrix were assumed to be the same as for the buffer.

Where the shear modulus, G, was required, the following expression was used:

$$G = \frac{E}{2(1+\upsilon)}$$

The coefficients of thermal expansion, α, used are given in Table 10. The coefficient of thermal expansion of the SiC matrix was set to that of the SiC layer.

The thermal conductivities, k, of the materials given are presented Table 11.

The specific heat capacity, c_v, is given in Table 12.

The thermal creep correlations for the various components are given in Table 13. Where R is the universal gas constant; G_s is the mean linear intercept grain size; σ is the equivalent (or von Mises) stress; P is the fractional porosity; Q presents the activation energies; and the other constants are given in Table 14.

2.6. Modelling of matrix boundary conditions

In most TRISO models, the OPyC outer surface is typically treated as a free boundary. A similar technique has been used in few studies that include a matrix in that the boundary of the matrix is treated as being free. However, particles that do not dwell at the edge of the compact may not be experiencing this situation. To assess matrix shapes and constraints, a set of simulations have been performed to test implementation of constraints on the boundary of the matrix, covering the extremes of the boundaries of the matrix. The tests were on an AGR-2 UO_2 particle embedded in a graphite matrix ramped to full power. The constraints, which are referenced in Fig. 3 include:

- Case A: A cuboidal matrix with three outer surfaces free and three outer surfaces that share the sectioned plane with the TRISO particle with zero displacement in the direction perpendicular to the sectioned plane.
- Case B: TRISO particle constrained in a matrix block with the three outer surfaces constrained from moving perpendicular or parallel to the surface plane.
- Case C: The particle within a spherical matrix with a free circumferential face.
- Case D: The particle within a spherical matrix with the displacement and rotations set to zero in all directions.

Table 6
The density for each material in the model.

Material	Theoretical Density (g cm^{-3})	Reference
UO_2	10.97	[43]
Carbon (PyC and graphite)	2.26	[44]
SiC	3.22	[37]
Zirconia	5.65	[45]

Table 7
The porosity assumed for each layer of the TRISO fuel particle and matrix.

Region	Fractional Porosity, P	Reference
UO_2	0.010	[35]
Buffer	0.500	[35]
Inner & Outer PyC	0.200	[46]
SiC	0.006	[35]
Graphite Matrix	0.250	[47]
SiC Matrix	0.004	[48]

Table 8
The elastic modulus assumed for each layer of the TRISO fuel particle and matrix.

Material	Elastic Modulus, E, (GPa)		Reference
	Assumed Value	Correlation	
UO_2	Correlation used	$233.4(1-2.752P)(1-1.0915\times 10^{-4}T)$	[49]
Buffer	13	$34.5e^{-2.03P}$	[50]
PyC	25	$25.0(1-1.91P+0.91P^2)$	[51]
SiC	Correlation used	$460-0.04Te^{\left(-\frac{962}{T}\right)}$	[52]
Graphite	13	$25.0(1-1.91P+0.91P^2)$	[51]
Zirconia	Correlation used	$247.7-0.0174T$	[53]

Table 9
Poisson's ratio assumed for each layer of the TRISO fuel particle and matrix.

Region	Poisson's Ratio, υ	Reference
UO_2	0.32	[54,55]
Buffer	0.24	[50]
PyC & Graphite Matrix	0.33	[56,57]
SiC	0.21	[58]
Zirconia	0.31	[59]

3. Results & discussion

3.1. Effects of constraints of the matrix

Fig. 4 illustrates how the shape of the matrix and the applied mechanical boundary conditions affect the stress state of TRISO particles. In Case B (block-shaped matrix with fixed boundary conditions on the outer surface) and Case D (a spherical matrix), the TRISO coating layers were shown to crush the fuel kernel—an outcome not typically observed in micrographs of as-manufactured fuel, making these cases an implausible as a way of modelling TRISO particles embedded in a matrix.

In contrast, in the simulations with free outer surfaces (Case A and Case C) both resulted in relatively low stress levels in the surrounding matrix. However, the stress distributions were noticeably different between the two. In Case A, there were small stress concentrations at the free edges of the block, leading to a wider variation in radial stress within the matrix material. Additionally, Case A showed a greater variation in hoop stress in the SiC coating layer compared to Case C. Thus, all subsequent simulations involving an encapsulated matrix used the boundary conditions from Case C.

3.2. Evolution of stress state during AGR-2 TRISO particle manufacture

Fig. 5 describes the stress state in each layer during the manufacturing process for a fully-bonded TRISO particle, prior to its sintering into a matrix. After the buffer deposition, tensile radial stresses in the kernel reached +17 MPa and compressive radial stresses of −14 MPa were seen in the buffer. The most extreme stresses are the residual

Table 10
The coefficient of thermal expansion assumed for each layer of the TRISO fuel particle and matrix.

Region	Coefficient of Thermal Expansion, α (K^{-1})	Reference
UO_2	$9.802 \times 10^{-6} + 5.41 \times 10^{-10}T + 1.317 \times 10^{-12}T^2$, $T < 973K$, $1.179 \times 10^{-5} + 4.858 \times 10^{-9}T + 3.65GOO7 \times 10^{-12}T^2$, $T \geq 973K$,	[60]
Buffer	3.5×10^{-6}	[50,54]
PyC	5.5×10^{-6}	
SiC Layer & Matrix	$(-1.8276 + 0.0178T - 1.5544 \times 10^{-5}T^2 + 4.524610^{-8}T^3) \times 10^{-6}$	[37]
Graphite Matrix	5.9×10^{-6}	[61]
Zirconia	1.1×10^{-5}	[62]

Table 11
The thermal conductivity for each layer of the TRISO fuel particle and matrix and the assumed value at 1023 K.

Material	Thermal Conductivity, k (W m^{-1} K^{-1})		Reference
	Assumed Value	Assumption	
UO_2	3.0	Low-irradiation fuel (0.2 MWd/tUO_2) at 1000 °C	[63]
Buffer Inner PyC Outer PyC	10.5 11.9 8.6	$10.98222\left(\frac{1-P}{1+2P}\right) + 0.00444$	[50]
Graphite Matrix	80.6	$\frac{2T}{2.15 \times 10^{-2}T + 5.56 \times 10^{2}} + \frac{1}{1.325.08119 \times 10^{-4}}$	[61]
SiC & Matrix	166.0	$3.91112 \times 10^{-2}e^{2.24732 \times 10^{-2}T}$	[50]
Zirconia	1.9	N/A	[64]

Table 12
The specific heat capacity for each layer of the TRISO fuel particle and matrix.

Region	Specific Heat Capacity, c_v (J kg^{-1} K^{-1})	Reference
UO_2	250	[65]
Buffer	500	
Inner PyC	500	
SiC Layer	1200	
Outer PyC	500	
SiC Matrix	1700	
Graphite Matrix	1200	[61]
Zirconia	400	[66]

Table 13
Thermal creep correlations for each layer of the TRISO fuel particle and matrix.

Region	Thermal creep rate (s^{-1})	Reference
UO_2	$\dot{\varepsilon} = \frac{C_1 \sigma e^{\frac{-Q_1}{RT}}}{(C_2 - P)G_S^2} + \frac{C_3}{C_2 - P}\sigma^{4.5}e^{\frac{-Q_2}{RT}}$	Hagrman et al. [55] which is based on Bohaboy et al. [67]
Buffer	No thermal creep	[68]
Inner PyC	No thermal creep	[68]
SiC Layer	$\dot{\varepsilon} = A\left(\frac{\sigma}{G}\right)^n e^{\frac{-Q}{RT}}$ Where $G = G_0 - \Delta G.T$	[10]
Outer PyC	No thermal creep	[68]
SiC Matrix	$\dot{\varepsilon} = A\left(\frac{\sigma}{G}\right)^n e^{\frac{-Q}{RT}}$	[10]
Graphite Matrix	No thermal creep	[61]
Zirconia	Deemed negligible for simulation case based on Zhu et al. [69]	[69]

stresses at the end of manufacture. The most significant residual stress components at the end of manufacture are a compressive hoop stress of −445 MPa in the SiC; a tensile stress of approximately 246 MPa in the kernel; and a tensile radial stress of 146 MPa in the buffer. For context, the fracture stress of UO_2 is estimated to be around 90–110 MPa [70] at the operating temperature range of the manufacturing process. The

Table 14
Constants for thermal creep correlations.

Material	Constant	T ≤ 1873 K	T > 1873 K
SiC	A	71.61	1.36×10^7
	n	2.3	3.7
	Q (J mol^{-1})	1.74×10^5	1.74×10^5
	G_0 (MPa)	$G = G_0$	$G = G_0$
	$\Delta G(MPaK^{-1})$	23	23
UO_2	C_1	3.92×10^{-9} s^{-1} $MPa^{-4.5}$	
	C_2	0.123	
	C_3	2.0391 s^{-1} $MPa^{-4.5}$	
	C_4	9.5×10^{-2} $MPa^{-4.5}$	
	Q_1	3.766×10^5 J mol^{-1}	
	Q_2	5.523×10^5 J mol^{-1}	
	G_s	$(1.30 - 1.36) \times 10^{-5}m$	
	P	1.003×10^{-2}	

fracture strength of the buffer has been traditionally assumed to be low (<50 MPa) [50]. However, recent studies by Mauseth et al. [71] have shown the buffer ultimate tensile strength can exceed ~138 MPa. Taken together, this would suggest that cracking is likely to occur in the kernel or delamination of the kernel/buffer interface during the cool down from TRISO manufacture or both failures occurring simultaneously. The simulation suggests that potential kernel fracture occurring 30–40 min into the cooldown of the particle after deposition. The implication is that when this discontinuity occurs within the particle, the SiC layer would already be in a state of tangential pre-compression between −133 and −168 MPa. Similarly, kernel/buffer interface delamination may occur 21–57 min into the cooldown with the SiC layer already in tangential pre-compression ranging from −106 to −225 MPa.

3.3. Evolution of stress state during matrix sintering phase of manufacture

Figs. 6 and 7 present the radial and hoop stress after manufacture of the singular particle until the particle is ready for its service life. As with the initial manufacturing process of the singular particle, the most extreme stresses are found at the end of manufacture of the SiC fuel compact, indicating that fracture model developments may consider the results at the end of the manufacturing transient. In contrast, for particles encapsulated in a graphite matrix, the most extreme stresses occur after the warm pressing stage, where compressive hoop stresses in the SiC layer reached −738 MPa. To isolate the influence of the matrix from the applied sintering conditions, additional simulations were conducted using bare TRISO particles (i.e., without matrix encapsulation) subjected to the sintering conditions associated with both graphite and SiC matrices. The results of these simulations are shown in Fig. 6 (b and d) and Fig. 7(b and d). In the case of the bare particle with associated sintering conditions of graphite applied, the stresses observed became more modest where the most extreme stresses were compressive hoop stresses in the SiC coating layer reaching −628 MPa. When SiC sintering conditions were applied to a bare particle, the resulting stresses were lower compared to the particle in the matrix. Notably, hoop stresses in the SiC coating layer also became tensile, reaching +81 MPa after the hot press ramp up — an effect not seen in particles encapsulated within a

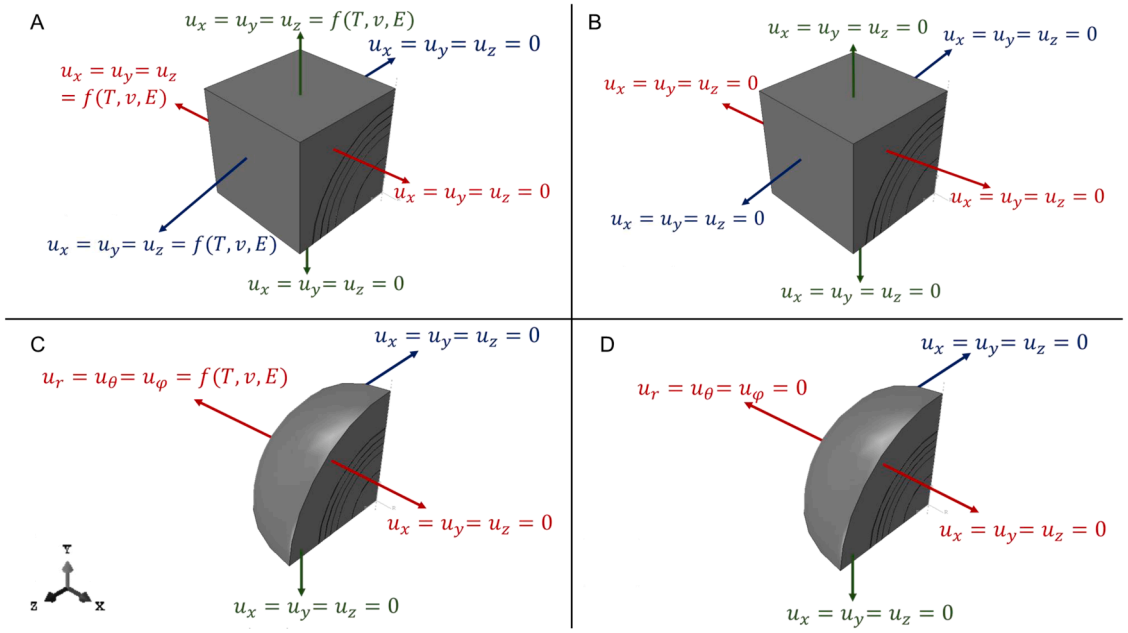

Fig. 3. Boundary conditions (BCs) applied to the matrix in cases A-D with T,v and E representing the thermal and elastic material properties; **r**, $\boldsymbol{\theta}$,$\boldsymbol{\varphi}$ representing the radial, polar and azimuthal axis.

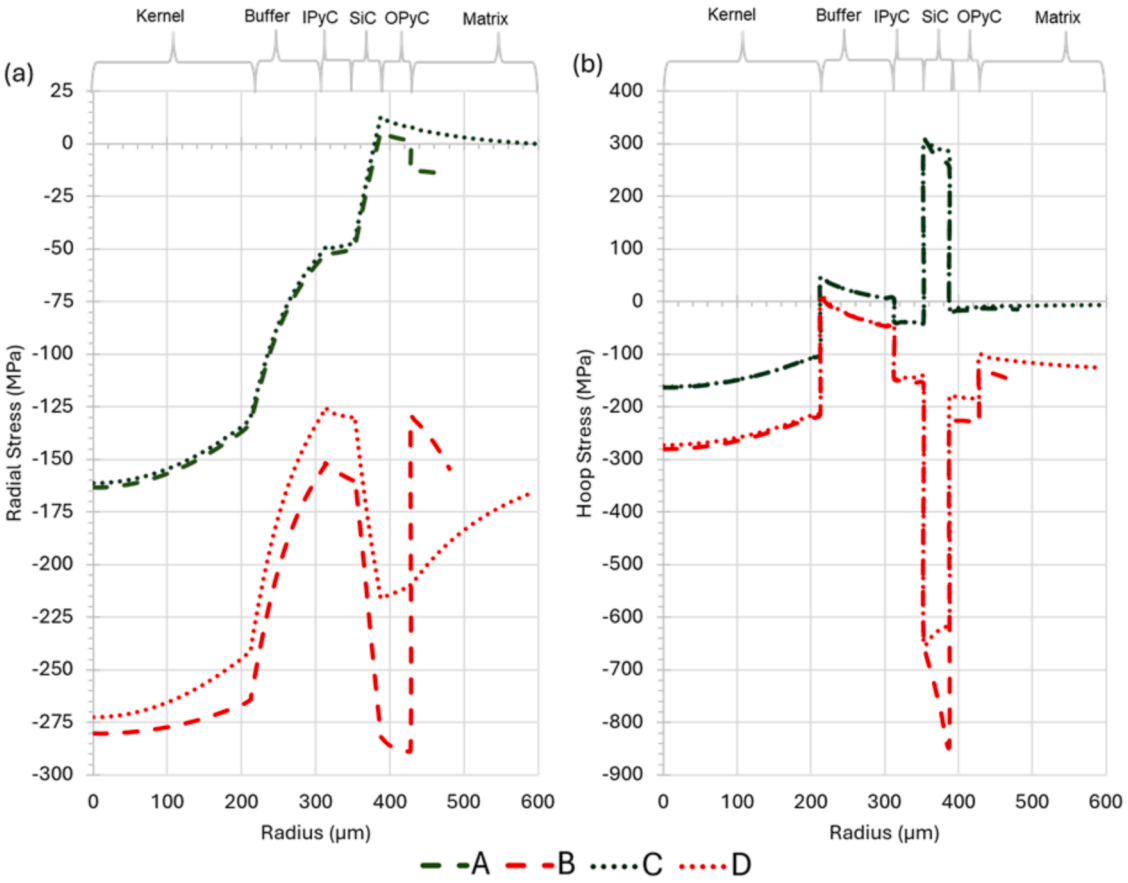

Fig. 4. (a) Radial and (b) hoop stress profile of particle embedded in matrices of different shape and boundary constraints of encapsulating matrix. Case A and Case C are the block-shaped matrix and spherical matrix respectively with free outer surfaces. Case B and Case D are the block-shaped matrix and spherical matrix respectively with fixed BCs on the outer surface.

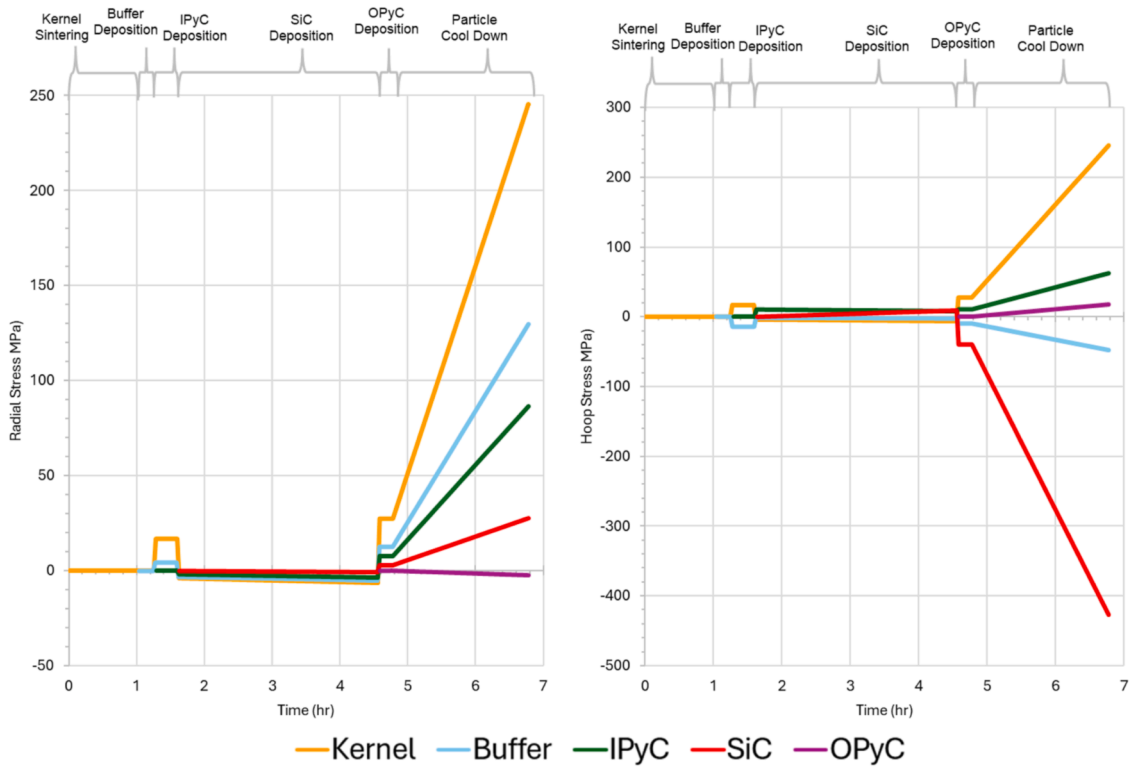

Fig. 5. The radial and hoop stress during manufacture of the TRISO particle (AGR-1 UO_2 kernel). The stress quoted is for positions at the centre of each region.

SiC matrix, where hoop stresses remained compressive throughout the sintering transient. These results shows that both the inclusion of the matrix and the sintering conditions associated with its inclusion play a role in the particle stress state during manufacture.

3.4. Residual stress state after manufacture

The trend in the radial and hoop stresses predicted in this study presented in Fig. 8 are similar to those predicted by Battistini et al. [10] and Montoya et al. [15]. Whilst the stresses in the kernel are similar to those predicted by Battistini et al. [10], the predicted hoop stresses in the SiC and OPyC are closer to those reported by Montoya et al. [15].

While the thermal and elastic properties used in this study are very similar to those in previous studies, they are not identical. The plasticity model employed here is consistent with that used by Battistini et al. [10],whereas Montoya et al. [15] did not incorporate any plastic features. The deposition temperatures used in Battistini et al. [10], are representative of the fabrication of a German AVR LEU-UO_2 TRISO particle, while this study and the work by Montoya et al. [15] adopts temperatures representative of the AGR-2 CVD process. The contact interaction models also differ: this study uses a cohesive contact approach that allows rotational degrees of freedom, which are constrained with the "Tie" contact formulation on Abaqus used in Battistini et al. [10]. Additionally, Battistini et al. [10] modelled the particle with the AGR-1 dimensions, which have significantly smaller kernels and different coating thicknesses compared to the AGR-2 particles used in both this study and in Montoya et al. [15].

The inclusion of the matrix and different sintering conditions had a moderate impact on the radial stresses experienced in the kernel and TRISO layers. The only key difference was the compressive stresses predicted in the OPyC layer and matrix of the graphite encapsulated particle which reached −15 MPa. In the other cases, stresses were miniscule, never exceeding 5 MPa. The most extreme stresses are the compressive hoop stresses reaching −540 MPa in the SiC layer of the graphite encapsulated matrix as compared to −493 MPa when applying graphite sintering conditions to a bare particle. The result shows modest differences ($< \pm 11$ MPa) between the SiC encapsulated matrix, where stresses in the SiC layer reached −446 MPa and the bare particle with and without SiC matrix sintering operations applied to the bare particle. The results highlight that after the TRISO particle manufacture, the sintering conditions experienced by the fuel affect the residual stresses in the coating layers, more particularly the AGR-2 sintering conditions and the inclusion in a graphite matrix.

3.5. TRISO fuel power ramp

Fig. 9 demonstrates the radial and hoop stresses in the TRISO fuel after the initial power ramp with the inclusion of manufacturing-induced residual stresses. The overall stress trends closely resemble those seen in the residual stress state of the particle (both bare and encapsulated in a matrix), with some notable differences—particularly in the fuel kernel. Within the UO_2 kernel, the thermal gradient during the power ramp produces a significant stress variation (up to 72 % change) between the kernel centreline and its outer surface. In the inner and outer PyC layers, no significant stresses are seen after the inclusion of the matrix. Stresses in the SiC layer became more extreme when the power ramp was modelled with the inclusion of a SIC matrix, reaching −388 MPa as compared to −222 MPa in a graphite matrix. This is despite, the stresses in the SiC coating layer of the SiC-matrix encapsulated particle being less compressive when compared to the SiC layer of the particle in graphite matrix after the manufacture of the particle.

The reason for this phenomenon is earlier explained by the minimal tensile stresses seen after the initial rise to power without the inclusion of as-manufactured stresses in Fig. 10. Fig. 10 shows the radial and hoop stress in both bare and matrix encapsulated particle fuel at the end of the initial rise to power, excluding any residual manufacturing stresses. It also shows that the effects of the temperature-dependence of the differences in thermal expansion of the particle layers are important since the temperature difference between the TRISO cool down and the initial power ramp is only double, indicating that without the temperature-

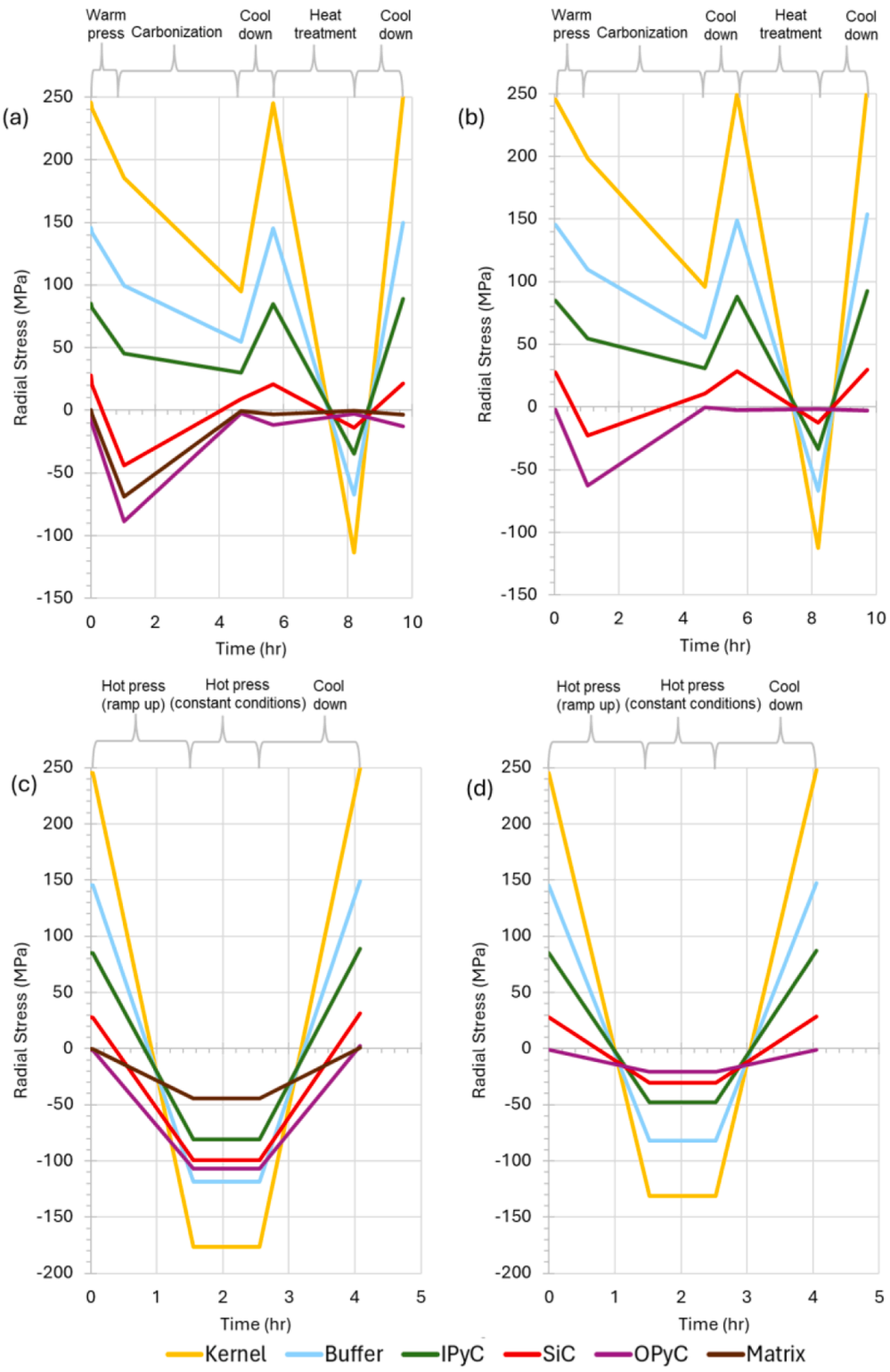

Fig. 6. Radial stress during sintering phase of manufacture of the TRISO particle in (a) Graphite with sintered matrix (b) Graphite sintering conditions without matrix (c) SiC sintering conditions with matrix and (d) SiC sintering conditions without matrix. The stress quoted is for positions at the centre of each region.

dependence in the model, the predictions will drastically under-estimate the compressing effects of the manufacturing conditions compared to the tensile stresses induced by the power ramp on the SiC layer.

The results from Fig. 10 also indicate that, in the absence of residual stresses, encasing the TRISO particle in a graphite matrix has a less significant effect compared to encapsulation in a SiC matrix. For radial compressive stresses, the SiC-encapsulated particle consistently exhibited the highest levels, followed by the bare particle, with the graphite-encapsulated particle showing the lowest. Notable differences were seen in the matrix with the SiC encapsulated particle experiencing hoop tensile stresses of up to +73 MPa and the graphite matrix in compression of up to −16 MPa. The SiC coating layer of the SiC-encapsulated particle experienced hoop stresses of only +49 MPa, 229 MPa lower than the hoop stress in the bare particle which were only 10

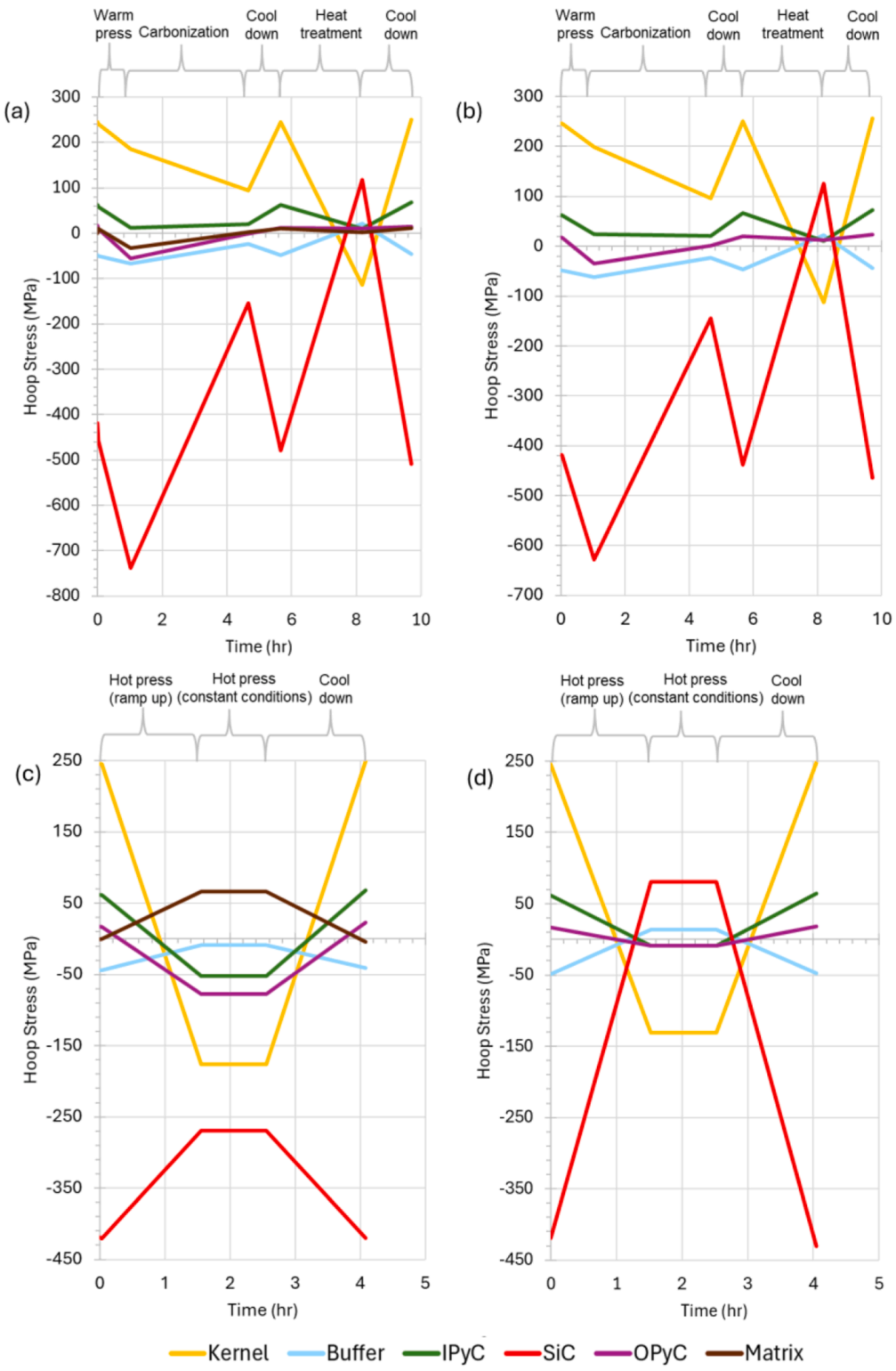

Fig. 7. Hoop stress during sintering phase of manufacture of the TRISO particle in (a) Graphite with sintered matrix (b) Graphite sintering conditions without matrix (c) SiC sintering conditions with matrix and (d) SiC sintering conditions without matrix. The stress quoted is for positions at the centre of each region.

% less than the hoop stress in the graphite-encapsulated particle. Finally, tensile radial stresses were only predicted in the OPyC layer of both the bare and graphite-encapsulated particles, as well as within the graphite matrix itself.

The results suggest that the inclusion of the particle in a SiC matrix offers multiple benefits to the structural integrity of TRISO fuel as:

i. The far greater compressive stresses after the power ramp will provide greater allowance of the SiC layer to respond to internal gas pressure in the particle.
ii. All hoop stresses in the TRISO layers were compressive with the matrix and kernel being in tension with more probability of radial cracks in the SiC matrix. Some SiC-matrix TRISO particle show cracking in the matrix as shown in Fig. 13.

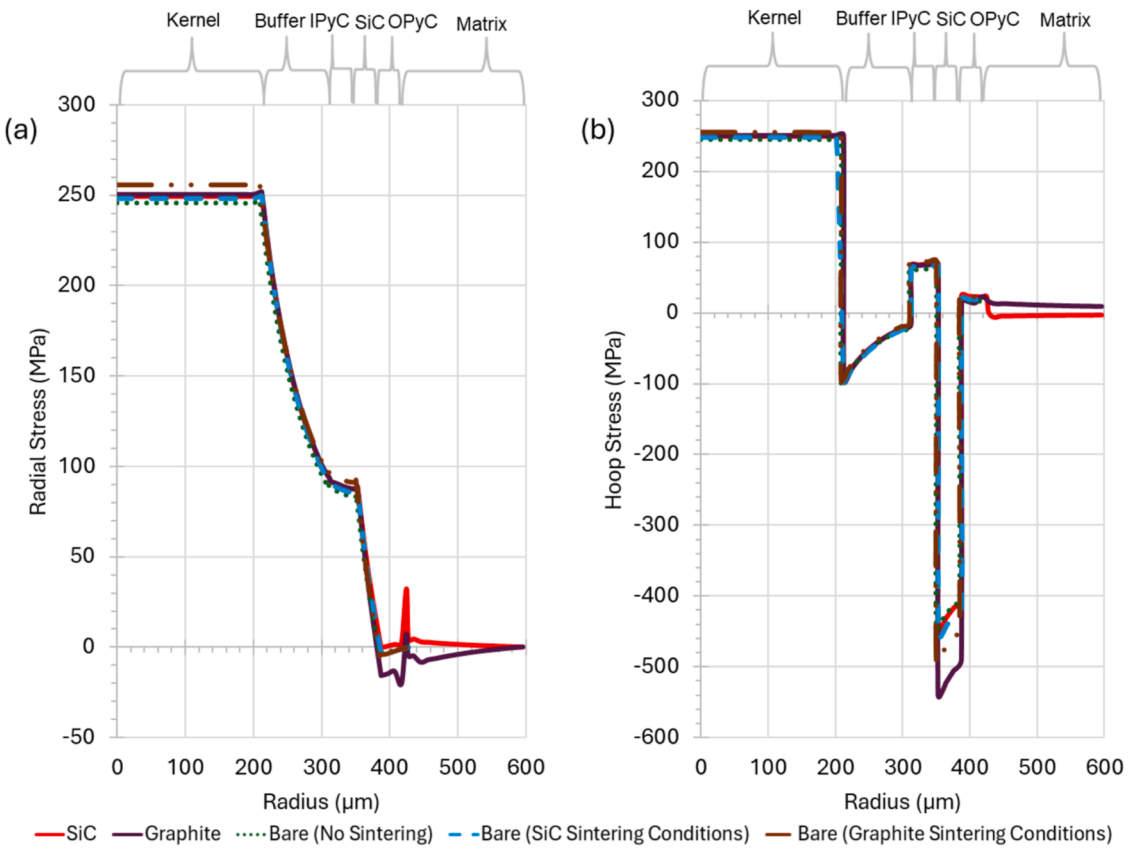

Fig. 8. The residual (a) radial and (b) hoop stress in bare and matrix encapsulated TRISO fuel at the end of manufacture.

These benefits indicate that the inclusion of a TRISO particle in a SiC matrix may lead to enhanced TRISO fuel performance. At a lower packing fraction, we hypothesize that a TRISO particle encapsulated in a SiC matrix will experience greater compressive hoop stresses in the SiC coating layer as the larger volume fraction of the matrix material will amplify its influence on the particle's stress profile. An additional set of simulations were carried out to demonstrate this, the results of which are presented in Fig. 11 which shows that increasing the packing fraction of the fuel may reduce the compressive stresses in the SiC layer and increase the tensile stresses in the SiC matrix. A similar trend of reduced compressive stresses in the SiC coating layer with increased packing fraction in a graphite-encapsulated particle is presented in Fig. 12. On the other hand, the effect of packing fraction on the graphite matrix was negligible. It is important to re-emphasize that the results presented in this study on packing fraction do not consider the inter-particle stress effects but are only limited to the effect of the volume of the matrix material due to packing fraction changes. Inter-particle stress interactions may further amplify or negate these effects as demonstrated in the work of Boer et al. [16].

It is important to re-emphasize that the predictions in this study are highly sensitive to the material properties employed. Currently, there is no consensus on these material properties over the full range of manufacturing and operating conditions, as they are influenced by variances in manufacturing tolerances as well as molecular and microstructural evolutions that remain incompletely understood. The sensitivities of the predictions to the wide range of reported correlations and property values have not been fully explored. Moreover, this model does not account for graphitization of the PyC layer or the associated changes in elastic properties, especially at elevated temperatures, which could affect the predictions in this study. Nevertheless, model validation attempts were made using the selected material properties. Also, the sensitivity of the stress distribution predictions to the elastic properties of the buffer layer were investigated.

3.6. Model validation and comparison to experimental results

In this work, the USNC sample of Leide et al. [9] was used for model validation as this is the only study in the open literature that experimentally quantifies the residual stresses in the coating layers that could be found. The experiments were also carried on a TRISO particle with a 790 μm diameter zirconia-kernel with layer thicknesses of 87 μm, 36 μm, 40 μm, 32 μm for the buffer IPyC, SiC and OPyC respectively. These same dimensions were used to develop another model applying the same fabrication methods for the AGR-2 particles that were described earlier.

3.6.1. Sensitivity of prediction to buffer elastic properties

For a surrogate zirconia-kernel model, with all interfaces bonded, a sensitivity study was carried out on how the buffer porosity and Poisson's ratio affect the residual stress in the SiC layer, the results of which are shown in Fig. 14. As a first approximation, the influence of porosity was incorporated into the model by varying the elastic modulus of the buffer using the correlation from Petti et al. [50], presented in Eq. (6),

$$E = 34.5e^{-2.03P} \tag{6}$$

Where E is the elastic modulus and P represents the fractional porosity of the buffer. It should be noted that this correlation does not account for high-temperature heat treatment of the buffer, which is likely to induce microstructural changes such as graphitization. Also, the heterogenous nature of the pores as well surface roughness which may play a role in the residual stresses were not factored in this study.

Fig. 14 shows that the residual stress is highly sensitive to the porosity of the buffer, with a greater sensitivity at lower Poisson's ratios. An explanation for this is that a denser buffer will be stiffer, allowing for more compression in the buffer that will leave the PyC layers in more

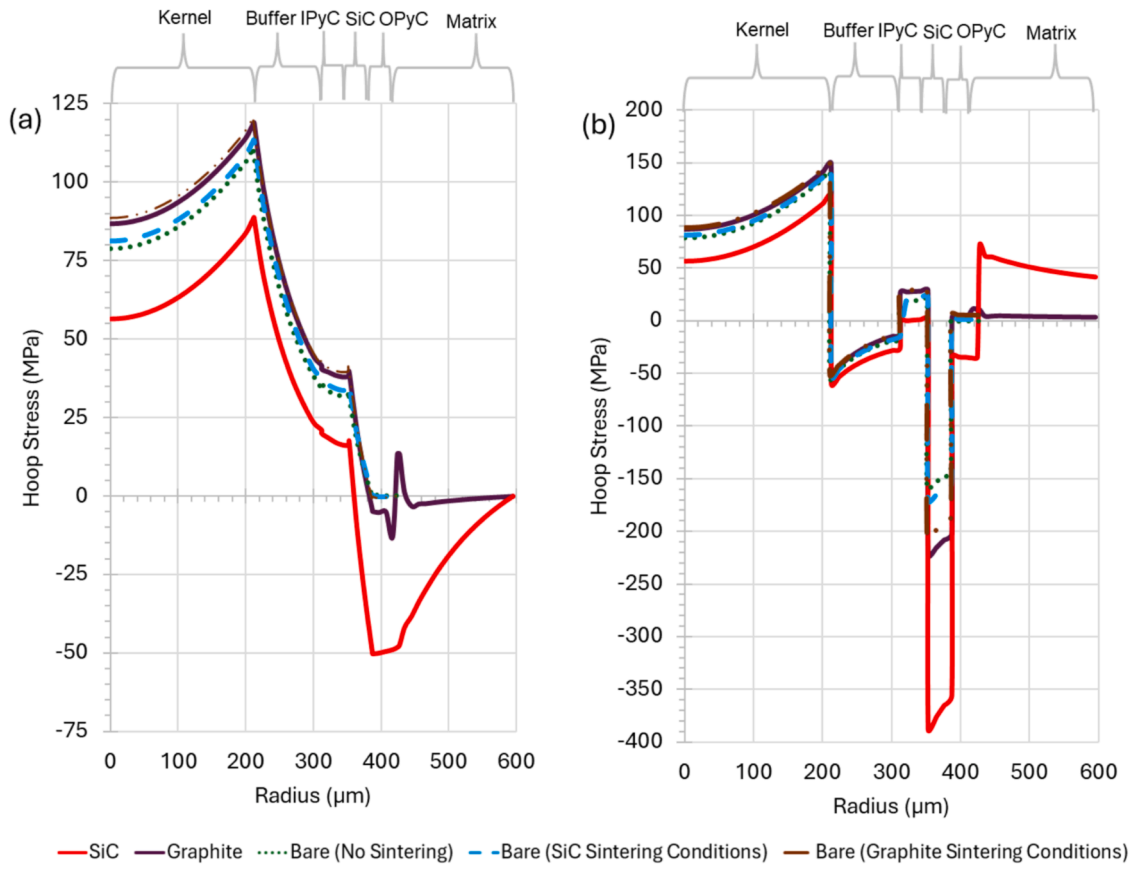

Fig. 9. (a) Radial and (b) hoop stress after initial rise to power of a bare TRISO particle and a particle encapsulated in a graphite or SiC matrix including residual stresses.

tension, allowing for higher compressive stresses in the SiC layer. Using the typical Poisson's ratio of the buffer of ~0.24, the residual stresses at a buffer porosity of 57 % corroborate with the values reported in Leide et al. [9]. This porosity is similar to the theoretical porosity of the buffer of 50 % [75]. However, Griesbach et al. [26] showed the heterogeneity of the porosity of the buffer layer with an average porosity of 14 % that would suggest residual stresses over 1 GPa without kernel/buffer delamination. There is no uniformity in literature on the characterisation of the buffer as quality control standards for this layer are typically low as it has been traditionally considered as an inert "sponge". This sensitivity study adds to the relevance of the buffer material elastic characterisation in the particle's fuel performance modelling, given its importance in the buffer/iPyC interface delamination due to irradiation [76]. The higher predicted hoop stresses in the SiC layer of the surrogate model compared to the AGR-2 particles is as a result of several factors which include differences in the coefficient of thermal expansion and elastic properties of the kernels. However, differences in dimensions between the AGR-2 particle and USNC surrogate particle play the most significant role. In a fully bonded model, a larger and stiffer kernel would be in greater tension, leading to greater tension in the IPyC layer and greater compression in the SiC layers. This emphasizes the need for using surrogate particles with similar dimensions when investigating TRISO particles for higher fidelity results.

3.6.2. *Validation in contest of delamination hypothesis*

Battistini et al. [10] hypothesized that debonding will occur at the kernel/buffer interface due to high tensile stresses in the kernel, buffer and at their shared interface. Our predictions also showed hoop stresses up to +160 MPa at the kernel/buffer interface sufficient to break the interfacial bonds. In the open literature, it is normally assumed that interfacial strengths are less than or equal to the strength of the adjoined material with the lower fracture strength [77,78]. Recent studies of TRISO particles negate this typical assumption. Seibert et al. [27] predicted bond strengths of up to 1 GPa, considerably higher than the PyC and SiC layers. Huang et al. [79] measured interfacial strengths of these interfaces that are about twice the nominal SiC strength published in Snead et al. [37]. Although dislocation behaviour and size effects (Hall-Petch effects) may indicate higher measurement values since the referenced tests were carried out on the micro-scale, the kernel/buffer bond strength may still be higher than its expected strength which is assumed to be lower than the buffer strength. Moreover, the predicted stresses in the SiC for a fully delaminated kernel/buffer interface model of Battistini et al. [10] show results that are about seven times less than the values reported in Leide et al. [9]. In this study, tensile stresses up to +10 MPa in the SiC layer were predicted after complete kernel/buffer interfacial debonding. The higher tensile stresses in the kernel may also imply the kernel cracks before delamination of the kernel/buffer interface.

The reference tested TRISO particle shows debonding at the kernel/buffer interface with no delamination in any of the other layers as reported in Leide et al. [9]. It is unclear whether this debonding is partial or complete, but it appears to be partial as shown in Fig. 15. Thus, partial delamination simulations were conducted. The partial delamination simulations allowed for delamination in only a portion of the kernel/buffer interface during cooling of the particle. In the region of the interface that was not allowed to delaminate, the interfacial conditions of the model remained the same (as described in Section 2.4) while the region that was allowed to delaminate had a frictionless, hard, surface-to-surface contact interaction property. It is important to note that Leide et al. [9] measured the residual stress at a single location using strain relief, and neither the average stress nor the stress distribution along the radial planes was determined in the SiC layer. The

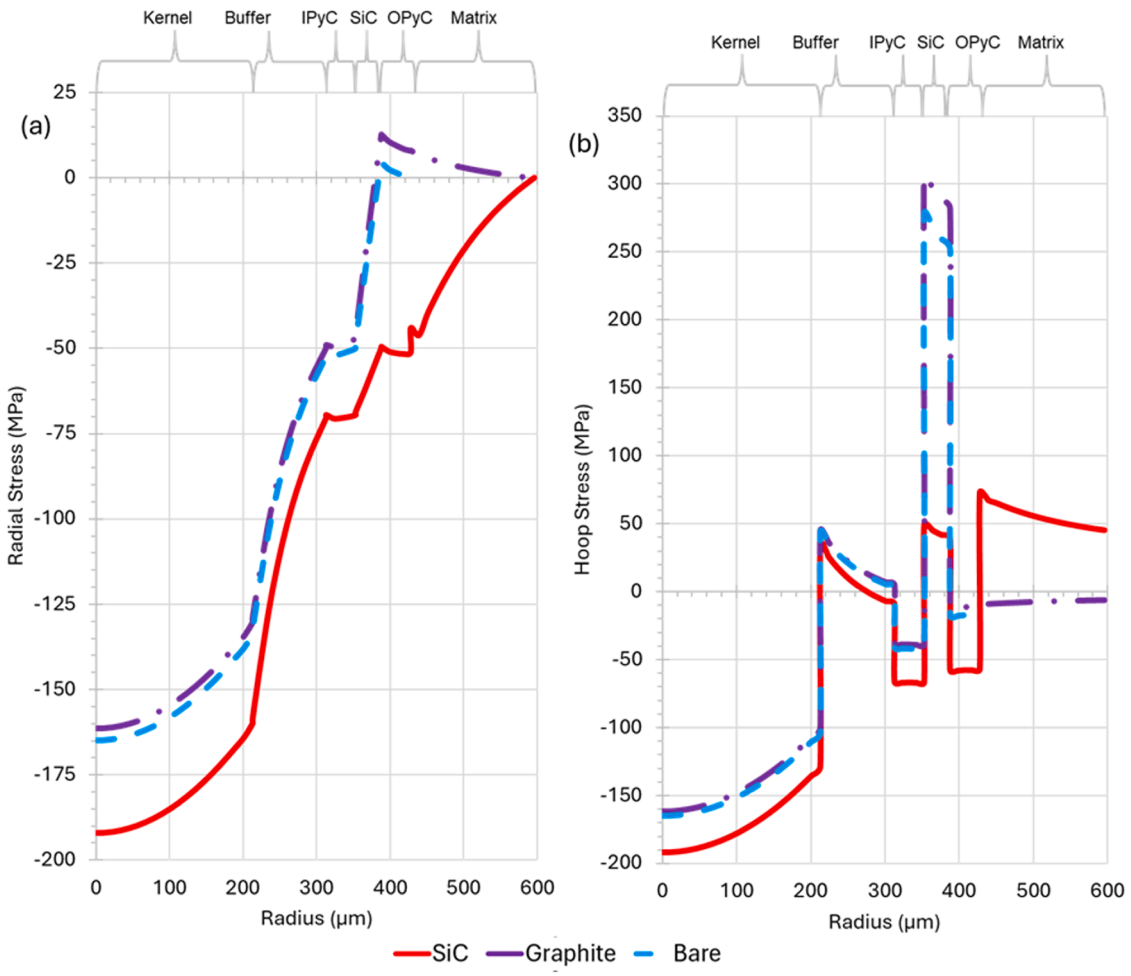

Fig. 10. (a) Radial and (b) hoop stress after initial rise to power of a bare TRISO particle and a particle encapsulated in a graphite or SiC matrix excluding residual stresses.

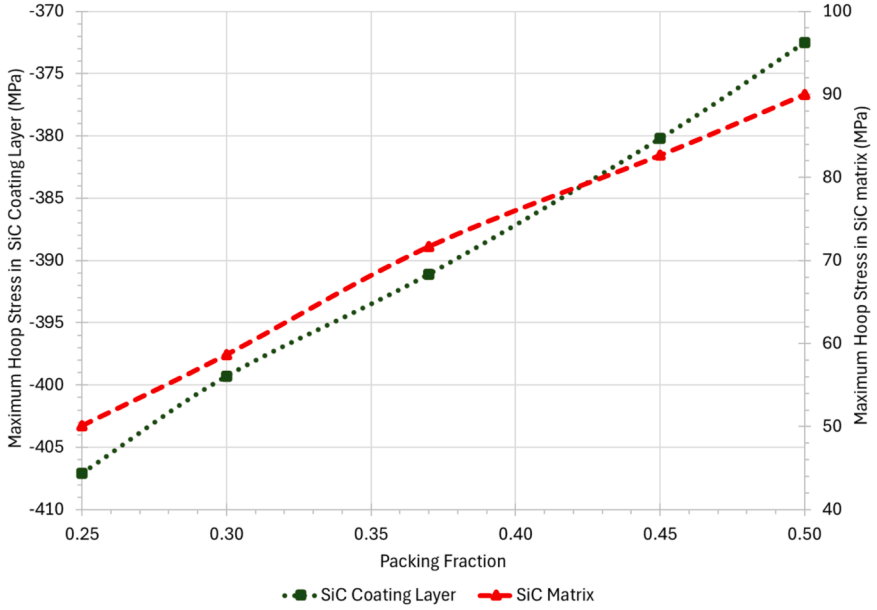

Fig. 11. Effect of packing fraction on the hoop stresses predicted in the SiC coating layer and SiC matrix after initial rise to power of a SiC matrix-encapsulated TRISO particle.

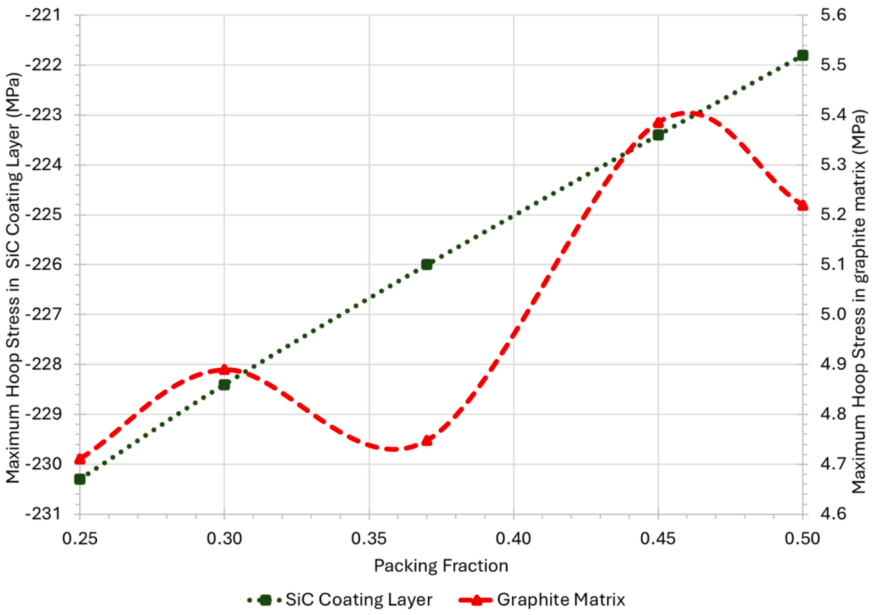

Fig. 12. Effect of packing fraction on the hoop stresses predicted in the SiC coating layer and graphite matrix after initial rise to power of a graphite matrix-encapsulated TRISO particle.

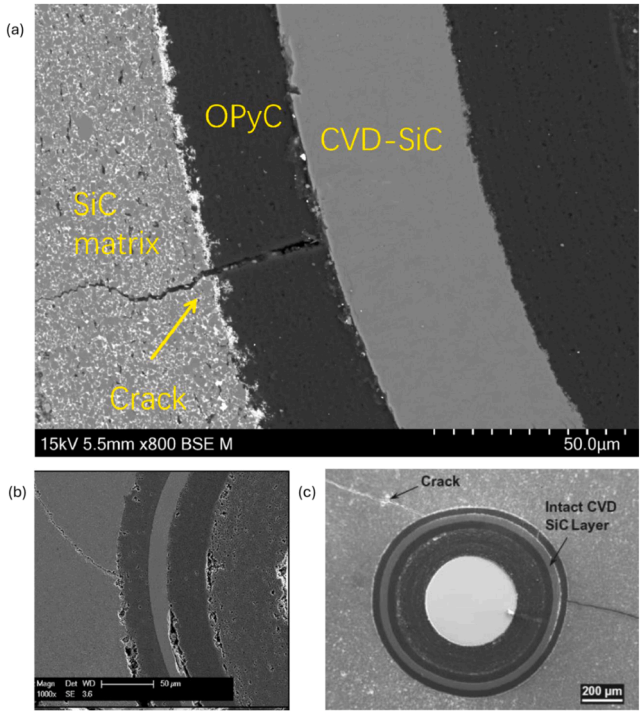

Fig. 13. Micrographs showing radial cracks in the SiC matrix of TRISO particles. (a) and (c) from Tan et al. [72] and Zhang et al. [73] respectively by permission of Elsevier under License Nos. 6050821358746 and 6050821271589 respectively. (b) from Lee et al. [74].

sectioning of the particle before the residual stress measurement may also have had a moderate impact on the stress state of the kernel and coating layers from the illustrative finite element model developed in their study.

The partial kernel/buffer interfacial delamination simulations results show an asymmetric stress distribution in Fig. 16. Fig. 16 shows that along different axes along the cutting plane, the stress distribution in the SiC layer ranges from tensile stresses of up to +54 MPa to compressive stresses as high as −546 MPa, located directly above the bonded region. In this model, kernel cracking may still occur due to stress concentrations close to the portion of the interface still in contact with the buffer. Kernel cracking phenomena is also apparent in the TRISO surrogate micrographs.

Qualitative residual stresses with EBSD are also in agreement with an evolution of strains that may range from tensile to compressive within the SiC layer as predicted in these studies [13,14]. As this model assumes a buffer porosity of 50 %, a lower porosity may lead to a higher compressive stress experienced in some zones of the SiC layer as Fig. 14 shows increased compression with a lower buffer porosity which was observed by Griesbach et al. [26]. The benchmark experimental case study is based on a particle manufactured on a laboratory scale. Industrial scale manufacturing may yield TRISO particles with lower or higher buffer porosities. It is important to note that debonding was allowed for 71 % of the kernel/buffer interface surface area. Simulations where debonding was allowed for a greater proportion of the interface showed a similar trend and values of the stress distribution. These simulation results show that the nature of the kernel/buffer delamination may play a very important role on the residual stress distribution of the particle. The results also strengthen the case for experimental measurements of the residual stress across different radial planes of the particle.

Although TRISO fuel performance is stochastic, the key takeaway from these analyses is that the stress variations caused by differences in the buffer material and its interfacial interactions can make an order of magnitude difference to the stresses experienced in the TRISO layers during service life. Therefore, the buffer characteristics play a crucial role in both reactor operation and the TRISO particle manufacturing process.

4. Conclusions

The conclusions from this work are as follows:
Matrix Material and Characteristic Sintering Conditions Effects

- The sintering conditions during TRISO particle fabrication significantly influence the residual stresses in the coating layers, particularly under AGR-2 sintering conditions and with the inclusion of a graphite matrix material.

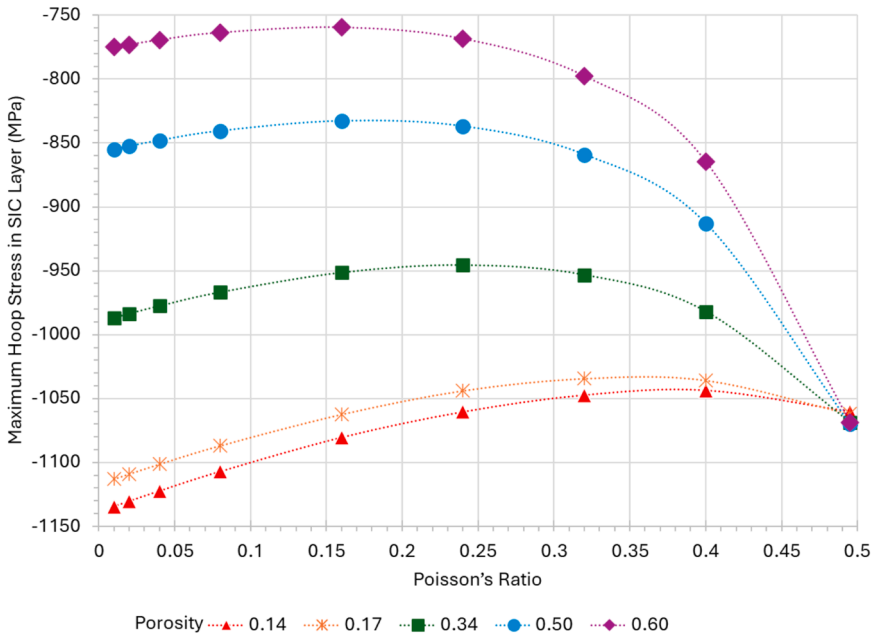

Fig. 14. Predicted average SiC layer hoop stress as a function of porosity and Poisson's ratio in the buffer in a fully bonded zirconia-Kernel TRISO particle.

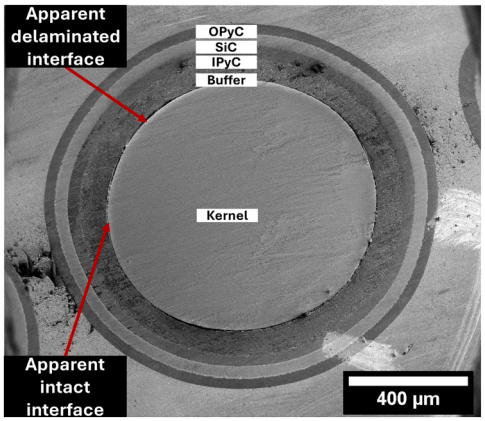

Fig. 15. Surrogate particle showing kernel/buffer delamination in various zones of zirconia surrogate TRISO particle. Reproduced from Leide et al. [9] under the terms of the Creative Commons CC-BY license.

- Compressive hoop stresses in the SiC layer reached −540 MPa in the graphite-encapsulated particle, compared to −493 MPa when graphite sintering conditions were applied to a bare particle.
- After sintering, the residual hoop stress in the SiC coating layer reached approximately −446 MPa in the SiC matrix, which is 94 MPa lesser than in the graphite matrix. However, after the initial power ramp, the predicted compressive hoop stress in the SiC layer was significantly greater in the SiC matrix (−388 MPa) compared to the graphite matrix (−222 MPa).
- Following the initial power ramp in both graphite and SiC matrix-encapsulated cases, an increase in unit packing fraction consistently resulted in reduced compressive stresses within the SiC coating layer. This effect was more pronounced for SiC-encapsulated particles than for graphite-encapsulated particles, with stress variations of 8.85 % and 3.76 %, respectively, across a packing fraction range of 0.25 to 0.50.

Possible Benefit of SiC Matrix

- It gives a significantly higher compressive stresses after the power ramp [−388 MPa in a SiC matrix compared to −222 MPa in a graphite matrix], potentially enhancing the SiC layer's ability to withstand internal pressure from fission gas release in the kernel.

Sensitivity of Residual Stresses to Buffer Elastic Properties

- The residual hoop stress experienced in the SiC layer of a fully-bonded model zirconia-kernel surrogate particle is highly sensitive to the porosity of the buffer, rising from a compressive stress of −0.77 GPa at a porosity of 0.60 to −1.06 GPa at a porosity of 0.14.

Partial Delamination at the Kernel/Buffer Interface

- A residual stress distribution of compressive hoop stresses of up to −546 MPa above a bonded region was predicted in the partial kernel/buffer delamination model with tensile stresses up to +54 MPa above the de-bonded region.
- The study re-enforces the importance of 3D models to capture interfacial characteristics when exploring asymmetrical features and phenomenon in TRISO fuel performance and the importance of obtaining more experimental data on residual stress of TRISO fuel.

Declaration

Mr Inyang-Udoh acknowledges support from the University of East Anglia, Faculty of Science PhD Studentship; Nuclear Innovation and Research Office; and the Department for Energy Security and Net Zero. Dr Battistini acknowledges financial support from the Engineering & Physical Sciences Research Council Nuclear Energy Futures Centre for Doctoral Training (grant EP/S023844/1) and the UK National Nuclear Laboratory. Dr Leide acknowledges support by the Royal Academy of Engineering under the Research Fellowship programme. Dr Haynes acknowledges support from Nuclear Innovation and Research Office; and the Department for Energy Security and Net Zero. The research presented in this paper was carried out on the High-Performance Computing Cluster supported by the Research and Specialist Computing Support service at the University of East Anglia.

Inyang-Udoh's contributions to this work include conceptualization, methodology, software, formal analysis, investigation, writing (original

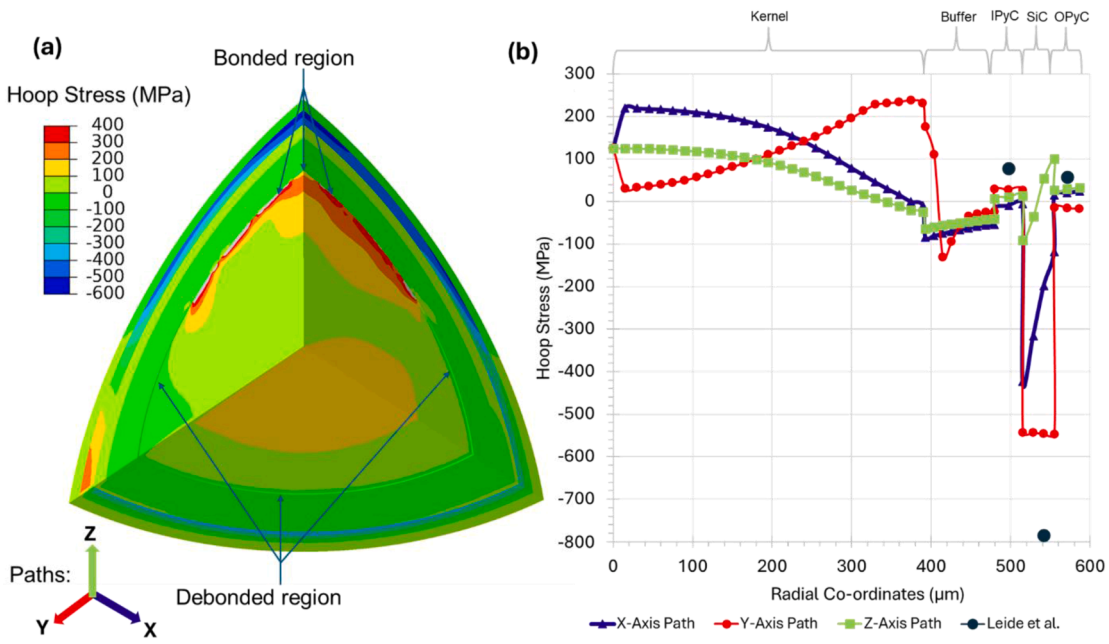

Fig. 16. Predicted hoop stress of the TRISO particle (a) showing partially debonded kernel/buffer interface (b) across different radial co-ordinate paths of TRISO particle.

draft) and visualisation. Dr Battistini's contributions to this work include writing (review and editing), methodology and formal analysis. Dr Jones's contribution to this work includes writing (review and editing). Dr Leide's contribution to this work includes writing (review and editing). Prof Wenman's contributions to this work include writing (review and editing). and supervision. Dr Haynes's contributions include writing (review and editing), supervision and funding acquisition.

CRediT authorship contribution statement

Udeme Inyang-Udoh: Writing – original draft, Visualization, Software, Methodology, Investigation, Formal analysis, Conceptualization. **Angelo Battistini:** Writing – review & editing, Methodology, Formal analysis, Conceptualization. **Lloyd Jones:** Writing – review & editing. **Alex Leide:** Writing – review & editing. **Mark R. Wenman:** Writing – review & editing, Supervision. **Thomas A. Haynes:** Writing – review & editing, Supervision, Funding acquisition.

Declaration of competing interest

The authors declare the following financial interests/personal relationships which may be considered as potential competing interests:

Dr Thomas A. Haynes reports financial support was provided by Nuclear Innovation and Research Office & Department for Energy Security and Net Zero. Mr Udeme Inyang-Udoh reports financial support was provided by Nuclear Innovation and Research Office & Department for Energy Security and Net Zero. Dr Angelo Battistini reports financial support was provided by Engineering and Physical Sciences Research Council. Dr Angelo Battistini reports financial support was provided by UK National Nuclear Laboratory. Dr Alex Leide reports financial support was provided by Royal Academy of Engineering. If there are other authors, they declare that they have no known competing financial interests or personal relationships that could have appeared to influence the work reported in this paper.

Acknowledgements

We appreciate the insightful feedback and guidance from Dr Dong Liu. We extend our gratitude to Dr Simon Franklin, for the invaluable review and support in funding acquisition for this work.

Data availability

Data will be made available on request.

References

[1] N.R. Brown, A review of in-pile fuel safety tests of TRISO fuel forms and future testing opportunities in non-HTGR applications, J. Nucl. Mater. 534 (2020) 152139, https://doi.org/10.1016/j.jnucmat.2020.152139, 2020/06/01/.
[2] Electric Power Research Institute, "Uranium oxycarbide (UCO) tristructural isotropic (TRISO) coated particle fuel performance: topical report EPRI-AR-1(NP)," 2019.
[3] D.A. Petti, J.T. Maki, J. Buongiorno, R.R. Hobbins, Key differences in the fabrication, irradiation, and safety testing of U.S. and German TRISO-coated particle fuel and their implications on fuel performance, United States, 2002-06-01, https://www.osti.gov/biblio/910651, 2002.
[4] J.W. McMurray, T.B. Lindemer, N.R. Brown, T.J. Reif, R.N. Morris, J.D. Hunn, Determining the minimum required uranium carbide content for HTGR UCO fuel kernels, Ann. Nucl. Energy 104 (2017) 237–242, https://doi.org/10.1016/j.anucene.2017.02.023, 2017/06/01/.
[5] T.M. Besmann, D. Shin, T.B. Lindemer, Uranium nitride as LWR TRISO fuel: thermodynamic modeling of U–C–N, J. Nucl. Mater. 427 (1) (2012) 162–168, https://doi.org/10.1016/j.jnucmat.2012.04.021, 2012/08/01/.
[6] T.A. Haynes, et al., Peridynamic modelling of cracking in TRISO particles for high temperature reactors, J. Nucl. Mater. 576 (2023) 154283, https://doi.org/10.1016/j.jnucmat.2023.154283, 2023/04/01/.
[7] O.Ö. Gülol, Ü. Çolak, B. Yıldırım, Performance analysis of TRISO coated fuel particles with kernel migration, J. Nucl. Mater. 374 (1) (2008) 168–177, https://doi.org/10.1016/j.jnucmat.2007.07.018, 2008/02/29/.
[8] G.K. Miller, D.A. Petti, J.T. Maki, D.L. Knudson, An evaluation of the effects of SiC layer thinning on failure of TRISO-coated fuel particles, J. Nucl. Mater. 355 (1) (2006) 150–162, https://doi.org/10.1016/j.jnucmat.2006.05.016, 2006/09/01/.
[9] A.J. Leide, et al., Measurement of residual stresses in surrogate coated nuclear fuel particles using ring-core focussed ion beam digital image correlation, Nucl. Mater. Energy 36 (2023) 101470, https://doi.org/10.1016/j.nme.2023.101470, 2023/09/01/.
[10] A. Battistini, T.A. Haynes, D. Shepherd, M.R. Wenman, Residual stresses in as-manufactured TRISO coated particle fuel (CPF), J. Nucl. Mater. 586 (2023) 154659, https://doi.org/10.1016/j.jnucmat.2023.154659, 2023/12/01/.
[11] D.G. Martin, An analysis of stresses created in the layers of coated fuel particles by temperature changes, in: *International Conference of Structural Mechanics and Reactor T*echnology, IASMiRT, 1975 [Online]. Available, https://repository.lib.ncsu.edu/server/api/core/bitstreams/a012a518-cd9e-4aaf-87a1-a70ce6ef5f74/content.

[12] L. Tan, T.R. Allen, J.D. Hunn, J.H. Miller, EBSD for microstructure and property characterization of the SiC-coating in TRISO fuel particles, J. Nucl. Mater. 372 (2) (2008) 400–404, https://doi.org/10.1016/j.jnucmat.2007.04.048, 2008/01/31/.

[13] R. Kirchhofer, B. Hansford, I.E. Reimanis, B.P. Gorman, Characterization of stresses in the SiC layer of TRISO coated nuclear fuels using Raman spectroscopy and EBSD, Microsc. Microcroanalysis 16 (2010), https://doi.org/10.1017/S1431927610058770.

[14] R. Kirchhofer, J.D. Hunn, P.A. Demkowicz, J.I. Cole, B.P. Gorman, Microstructure of TRISO coated particles from the AGR-1 experiment: siC grain size and grain boundary character, J. Nucl. Mater. 432 (1) (2013) 127–134, https://doi.org/10.1016/j.jnucmat.2012.08.052, 2013/01/01/.

[15] K.I. Montoya, E.G. Herbert, D.P. Schappel, C.M. Petrie, A.T. Nelson, T.J. Gerczak, Micromechanical response of SiC-OPyC layers in TRISO fuel particles, J. Nucl. Mater. 606 (2025) 155654, https://doi.org/10.1016/j.jnucmat.2025.155654, 2025/02/01/.

[16] B. Boer, A.M. Ougouag, J.L. Kloosterman, G.K. Miller, Stress analysis of coated particle fuel in graphite of high-temperature reactors, Nucl. Technol. 162 (3) (2008) 276–292, https://doi.org/10.13182/NT08-A3956, 2008/06/01.

[17] D. Schappel, G. Pastore, K.A. Terrani, Modeling interface debonding in coated fuel particles with BISON, Nucl. Sci. Eng. 196 (3) (2022) 276–284, https://doi.org/10.1080/00295639.2021.1955590, 2022/03/04.

[18] T. Changbing, J. Yongjun, L. Yuanming, Z. Yi, P. Hua, Preliminary research on the irradiation-thermal-mechanical coupling behavior simulation method of FCM fuel, Int. J. Adv. Nucl. React. Des. Technol. 1 (2019) 51–56, https://doi.org/10.1016/j.jandt.2019.10.002, 2019/01/01/.

[19] M. Cai, T. Cong, H. Gu, Multiphysics fuel performance modeling of dispersed TRISO-coated particle fuel plate under long-time normal condition and accident conditions, Nucl. Eng. Des. 415 (2023) 112725, https://doi.org/10.1016/j.nucengdes.2023.112725, 2023/12/15/.

[20] H. Wei, et al., Effects of the key parameters of TRISO particle buffer layer on in-pile thermo-mechanical behavior in FCM fuel pellets, J. Nucl. Mater. 551 (2021) 152977, https://doi.org/10.1016/j.jnucmat.2021.152977, 2021/08/01/.

[21] P. Demkowicz, S. Ploger, J. Hunn, J.S. Kehn, Ceramographic examinations of irradiated AGR-1 fuel compacts, United States, 2012-09-01, https://www.osti.gov/biblio/1072396, 2012.

[22] P.A. Demkowicz, AGR-1 Post irradiation examination final report, United States, 2015-08-01, https://www.osti.gov/biblio/1236801, 2015.

[23] P.A. Demkowicz, J.D. Hunn, D.A. Petti, R.N. Morris, Key results from irradiation and post-irradiation examination of AGR-1 UCO TRISO fuel, Nucl. Eng. Des. 329 (2018) 102–109, https://doi.org/10.1016/j.nucengdes.2017.09.005, 2018/04/01/.

[24] F.J. Rice, J.D. Stempien, Ceramography of irradiated tristructural isotropic (TRISO) fuel from the AGR-2 experiment, United States, 2016-09-01, https://www.osti.gov/biblio/1364473, 2016.

[25] J. Li, J. Sun, D. She, L. Shi, Influence of input data uncertainties on failure probability of TRISO-coated particle, Ann. Nucl. Energy 163 (2021) 108561, https://doi.org/10.1016/j.anucene.2021.108561, 2021/12/01/.

[26] C. Griesbach, T. Gerczak, Y. Zhang, R. Thevamaran, Microstructural heterogeneity of the buffer layer of TRISO nuclear fuel particles, J. Nucl. Mater. 574 (2023) 154219, https://doi.org/10.1016/j.jnucmat.2022.154219, 2023/02/01/.

[27] R.L. Seibert, B.C. Jolly, M. Balooch, D.P. Schappel, K.A. Terrani, Production and characterization of TRISO fuel particles with multilayered SiC, J. Nucl. Mater. 515 (2019) 215–226, https://doi.org/10.1016/j.jnucmat.2018.12.024, 2019/03/01/.

[28] C.M. Barnes, AGR-1 fuel product specification and characterization guidance, United States, 21, https://www.osti.gov/biblio/1494142, 2006.

[29] J.D. Hunn, AGR-2 fuel compacts information summary: prepared for the NRC MELCOR Project [Online]. Available, https://www.ornl.gov/publication/agr-2-fuel-compacts-information-summary-prepared-nrc-melcor-project-0, 2010.

[30] X. Yang, et al., Microstructure and mechanical properties evolution of thermal-treated SiC layer with fine grain size in TRISO particles, Mater. Sci. Eng.: B 287 (2023) 116096, https://doi.org/10.1016/j.mseb.2022.116096, 2023/01/01/.

[31] I. Kenzhina, et al., Study of morphological, structural, and strength properties of model prototypes of new generation TRISO fuels, Materials. (2022), https://doi.org/10.3390/ma15144741. PMID: 35888209; PMCID: PMC9317622.

[32] K.A. Terrani, et al., Fabrication and characterization of fully ceramic microencapsulated fuels, J. Nucl. Mater. 426 (1) (2012) 268–276, https://doi.org/10.1016/j.jnucmat.2012.03.049, 2012/07/01/.

[33] C. Ang, L. Snead, Y. Kato, A logical approach for zero-rupture fully Ceramic Microencapsulated (FCM) fuels via pressure-assisted sintering route, J. Nucl. Mater. 531 (2020) 151987, https://doi.org/10.1016/j.jnucmat.2020.151987, 2020/04/01/.

[34] P.J. Pappano, T.D. Burchell, J.D. Hunn, M.P. Trammell, A novel approach to fabricating fuel compacts for the next generation nuclear plant (NGNP), J. Nucl. Mater. 381 (1) (2008) 25–38, https://doi.org/10.1016/j.jnucmat.2008.07.032, 2008/10/31/.

[35] P.A. Demkowicz, D.A. Petti, K. Sawa, J.T. Maki, R.R. Hobbins, TRISO-coated particle fuel fabrication and performance, Compr. Nucl. Mater. Second Ed. 5 (2020) 256–333.

[36] L.P.R. Garcia, D.M. Pérez, C.R.G. Hernández, D.E.M. Lorenzo, and C.A. Lira, "Development of a methodology for the evaluation of the thermomechanical behavior of the TRISO fuel," 2017.

[37] L.L. Snead, T. Nozawa, Y. Katoh, T.S. Byun, S. Kondo, D.A. Petti, Handbook of SiC properties for fuel performance modeling, J. Nucl. Mater. 371 (2007) 329–377.

[38] J.J. Powers, B.D. Wirth, A review of TRISO fuel performance models, J. Nucl. Mater. 405 (1) (2010) 74–82, https://doi.org/10.1016/j.jnucmat.2010.07.030, 2010/10/01/.

[39] J.W. Pomeroy, et al., Thermal conductivity of SiC and PyC coatings in spherical nuclear fuel particles measured by nanosecond time domain thermoreflectance, J. Eur. Ceram. Soc. 44 (6) (2024) 3696–3704, https://doi.org/10.1016/j.jeurceramsoc.2024.01.024, 2024/06/01/.

[40] J.D. Hunn, G.E. Jellison, R.A. Lowden, Increase in pyrolytic carbon optical anisotropy and density during processing of coated particle fuel due to heat treatment, J. Nucl. Mater. 374 (3) (2008) 445–452, https://doi.org/10.1016/j.jnucmat.2007.10.003, 2008/03/15/.

[41] T. Wang, H. Li, S. Zhang, K. Li, W. Li, The effect of microstructural evolution on micromechanical behavior of pyrolytic carbon after heat treatment, Diam. Relat. Mater. 103 (2020) 107729, https://doi.org/10.1016/j.diamond.2020.107729, 2020/03/01/.

[42] T. Wang, et al., Dependence of mechanical properties on microstructure of high-textured pyrocarbon prepared via isothermal and thermal gradient chemical vapor infiltration, Compos. B: Eng. 192 (2020) 107982, https://doi.org/10.1016/j.compositesb.2020.107982, 2020/07/01/.

[43] S.G. Popov, V.K. Ivanov, J.J. Carbajo, G.L. Yoder, Thermophysical Properties of MOx and UO2 Fuels Including the Effects of Irradiation, Oak Ridge National Laboratory, 2000. ORNL/TM-2000/351.

[44] A.J. Savvatimskiy, Measurements of the melting point of graphite and the properties of liquid carbon (a review for 1963–2003), Carbon. N. Y. 43 (2005) 1115–1142.

[45] Y. Yin, J. Xu, M. Ji, L. Li, M. Chen, A critical review on sintering and mechanical processing of 3Y-TZP ceramics, Ceram. Int. 49 (2) (2023) 1549–1571, https://doi.org/10.1016/j.ceramint.2022.10.159, 2023/01/15/.

[46] G.K. Miller, D.A. Petti, J.T. Maki, and D.L. Knudson, "PARFUME theory and model basis report," *Idaho National Laboratory,* vol. INL/EXT-08-14497, 2009.

[47] E.S. Kim, J.S. Song, S.D. Hong, Y.W. Kim, Porosity of nuclear gade graphite, in: Transactions of the Korean Nuclear Society Spring Meeting, Jeju, Korea, 2012, pp. 15–16. *17-18 May 2012*.

[48] Y. Katoh, T. Koyanagi, J.L. McDuffee, L.L. Snead, K. Yueh, Dimensional stability and anisotropy of SiC and SiC-based composites in transition swelling regime, J. Nucl. Mater. 499 (2018) 471–479, https://doi.org/10.1016/j.jnucmat.2017.12.009, 2018/02/01/.

[49] L.J. Siefken, E.W. Coryell, E.A. Harvego, and J.K. Hohorst, "MATPRO - A library of materials properties for light-water-reactor accident analysis," *Idaho National Engineering and Environmental Laboratory,* 2001.

[50] D. Petti, P. Martin, M. Phélip, and R. Ballinger, "Development of improved models and designs for coated-particle gas reactor fuels," *Idaho National Engineering and Environmental Laboratory Bechtel BWXT Idaho, LLC,* vol. INEEL/EXT-05-02615, 2004.

[51] K.H. Park, J.Y. Park, J.H. Park, W.J. Kim, C.H. Jung, Y.W. Lee, A novel approach to the porosity evaluation of pyrolytic carbon layers in TRISO-coated fuel, in: Transactions of the Korean Nuclear Society Spring Meeting. Chuncheon, Korea, 2006. *May 25-26 2006*.

[52] J.J. Powers, B.D. Wirth, A review of TRISO fuel performance models, J. Nucl. Mater. 405 (2010) 74–82.

[53] E.Y. Fogaing, Y. Lorgouilloux, M. Huger, C.P. Gault, Young's modulus of zirconia at high temperature, J. Mater. Sci. 41 (22) (2006) 7663–7666, https://doi.org/10.1007/s10853-006-0593-7, 2006/11/01.

[54] T.A. Haynes, et al., Peridynamic modelling of cracking in TRISO particles for high temperature reactors, J. Nucl. Mater. 576 (2023). Art no. 154283.

[55] D.T. Hagrman, C.M. Allison, G.A. Berna, SCDAP/RELAP5/MOD 3.1 code manual: MATPRO, a library of materials properties for light-water-reactor accident analysis, United States, https://www.osti.gov/biblio/100327, 1995.

[56] R. Li, B. Liu, C. Tang, Modification in the stress calculation of PyC material properties in TRISO fuel particles under irradiation, J. Nucl. Sci. Technol. 54 (7) (2017) 752–760.

[57] W.F. Skerjanc, B.P. Collin, Assessment of material properties for TRISO fuel particles in PARFUME, Idaho National Laboratory (INL), Idaho Falls, ID (United States), United States, https://www.osti.gov/biblio/1874979, 2018.

[58] Y.D. Ha, F. Bobaru, Studies of dynamic crack propagation and crack branching with peridynamics, Int. J. Fract. 162 (2010) 229–244.

[59] W. Pabst, E.V.A. GregorovÁ, Effective elastic properties of alumina-zirconia composite ceramics - part 3. Calculation of elastic moduli of polycrystalline alumina and zirconia from monocrystal data, Ceram. - Silikaty 48 (2004), 04/01.

[60] D.A. Petti, M. Philippe, P. Mayeul, B. Ronald, Development of improved models and designs for coated-particle gas reactor fuels – final report under the International Nuclear Energy Research Initiative (I-NERI), United States, http://inis.iaea.org/search/search.aspx?orig_q=RN:39005110, 2004.

[61] T.R. Pavlov, et al., Examining the thermal properties of unirradiated nuclear grade graphite between 750 and 2500 K, J. Nucl. Mater. 538 (2020). Art no. 152176.

[62] H. Hayashi, T. Saitou, N. Maruyama, H. Inaba, K. Kawamura, M. Mori, Thermal expansion coefficient of yttria stabilized zirconia for various yttria contents, Solid. State Ion. 176 (5) (2005) 613–619, https://doi.org/10.1016/j.ssi.2004.08.021, 2005/02/14/.

[63] I.A.E. Agency, "Thermal conductivity of uranium dioxide," vol. Technical Report Series No. 59, 1966.

[64] R.J. Takahashi, J.M.K. Assis, F.P. Neto, D.A.P. Reis, Thermal conductivity study of ZrO2-YO1.5-NbO2.5 TBC, J. Mater. Res. Technol. 19 (2022) 4932–4938, https://doi.org/10.1016/j.jmrt.2022.07.037, 2022/07/01/.

[65] D. Schappel, K.A. Terrani, J.J. Powers, L.L. Snead, B.D. Wirth, Modeling the performance of TRISO-based fully ceramic matrix (FCM) fuel in an LWR environment using BISON, Nucl. Eng. Des. 335 (2018) 116–127.

[66] D.F. Zambrano, et al., Thermal properties and phase stability of Yttria-stabilized Zirconia (YSZ) coating deposited by Air Plasma Spray onto a Ni-base superalloy,

Ceram. Int. 44 (4) (2018) 3625–3635, https://doi.org/10.1016/j.ceramint.2017.11.109, 2018/03/01/.
[67] P.E. Bohaboy, R.R. Asamoto, A.E. Conti, Compressive creep characteristics of Stoichiometric uranium dioxide, United States, https://www.osti.gov/biblio/4716019, 1969.
[68] N. Tzelepi, "GIF TRISO Workshop," ed. Personal Communications, Manchester, UK, 2024.
[69] D. Zhu, R.A. Miller, Sintering and creep behavior of plasma-sprayed zirconia- and hafnia-based thermal barrier coatings, Surf. Coat. Technol. 108-109 (1998) 114–120, https://doi.org/10.1016/S0257-8972(98)00669-0, 1998/10/10/.
[70] M. Oguma, Microstructure effects on fracture strength of UO_2 fuel pellets, J. Nucl. Sci. Technol. 19 (12) (1982) 1005–1014.
[71] T. Mauseth, M.L. Dunzik-Gougar, S. Meher, I.J. van Rooyen, Determining the tensile strength of fuel surrogate TRISO-coated particle buffer, IPyC, and buffer-IPyC interlayer regions, J. Nucl. Mater. 583 (2023) 154540, https://doi.org/10.1016/j.jnucmat.2023.154540, 2023/09/01/.
[72] J. Tan, R. Huang, H.-T. Lin, M. Liu, B. Liu, R. Liu, Fully ceramic microencapsulated fuels with high TRISO particles loading capacity fabricated by gel-casting, J. Nucl. Mater. 581 (2023) 154449, https://doi.org/10.1016/j.jnucmat.2023.154449, 2023/08/01/.
[73] C. Zhang, et al., Preliminary numerical investigation of TRISO-matrix interface debonding characteristics in fully ceramic microencapsulated fuel, Ann. Nucl. Energy 159 (2021) 108338, https://doi.org/10.1016/j.anucene.2021.108338, 2021/09/01/.
[74] H.-G. Lee, D. Kim, J.Y. Park, W.-J. Kim, Sintering and characterization of SiC-matrix composite including TRISO particles, J. Korean Ceram. Soc. 51 (5) (2014), https://doi.org/10.4191/kcers.2014.51.5.418, 418-0.
[75] S.A. Ploger, P.A. Demkowicz, J.D. Hunn, J.S. Kehn, Microscopic analysis of irradiated AGR-1 coated particle fuel compacts, Nucl. Eng. Des. 271 (2014) 221–230, https://doi.org/10.1016/j.nucengdes.2013.11.036, 2014/05/01/.
[76] Z.M. Krajewska, J.D. Hales, W. Jiang, Analysis of buffer-IPyC separation in TRISO fuel particles, Ann. Nucl. Energy 199 (2024) 110338, https://doi.org/10.1016/j.anucene.2023.110338, 2024/05/01/.
[77] X. Wang, F. He, Z. Chen, A. Atkinson, Porous LSCF/dense 3YSZ interface fracture toughness measured by single cantilever beam wedge test, J. Eur. Ceram. Soc. 34 (10) (2014) 2351–2361, https://doi.org/10.1016/j.jeurceramsoc.2014.02.008, 2014/09/01/.
[78] K.T. Faber, A.G. Evans, Crack deflection processes—I. Theory, Acta Metall. 31 (4) (1983) 565–576, https://doi.org/10.1016/0001-6160(83)90046-9, 1983/04/01/.
[79] H. Huang, D. Liu, Residual stresses measurements, Personal Communication (2024).